VNIVERSITAT Ọ ⅅⅇ VALÈNCIA

DOCTORAL PROGRAMME IN PHYSICS

DOCTORAL THESIS

Capture and processing of 3D microscopic images through multi-perspective technology

Gabriele Scrofani

Supervisors: Dr. Manuel Martínez Corral
Dr. Genaro Saavedra Tortosa

Valencia   2020

D. Manuel MARTÍNEZ CORRAL y D. Genaro SAAVEDRA TOR-
TOSA, Catedráticos de Óptica, adscritos al Departamento de Óptica
y Optometría y Ciencias de la Visión de la Universitat de València,

CERTIFICAN que la presente memoria, *Capture and processing
of 3D microscopic images through multi-perspective technology*, re-
sume el trabajo de investigación realizado, bajo su dirección, por D.
Gabriele SCROFANI y constituye su Tesis para optar al Grado de
Doctor en Física por la Universitat de València.

Y para que conste, en cumplimiento de la legislación vigente, fir-
man el presente certificado en Valencia, a ocho de junio de dos mil
veinte.

Dr. Manuel Martínez Corral   Dr. Genaro Saavedra Tortosa

Aknowledgements

I would like to spend some lines of this Thesis to acknowledge all those persons that shared with me the effort in the development of this work and to those that made it possible for me, to reach this point in my career.

I definitely have to start with my two supervisors Manuel Martínez Corral and Genaro Saavedra Tortosa, who decided to expand their research group including an engineer, and gave me the chance to be that person. This opportunity, to work alongside with them, have been a great experience for me, but mostly an incredibly stimulus to my knowledge. Apart from the work side, where nothing can be regretted thanks to their help and passion in their research field, I surely have to acknowledge them the personal side, for the support in literally all the issues I had to face during these years. And mostly for the great time and laughs spent together and the funny stories shared during the last four years.

Then I would like to thank all the persons met through the *3D Imaging & Display* lab. of the University of Valencia. From those persons I worked with at the beginning like Jorge, prof. Juan Carlos Barreiro and prof. Jorge Garcia Sucerquia of the National University of Colombia, till all the researchers that helped me throughout the years of this Ph.D. like Min, Amir, Adrian, Anabel, Alejandro, Przemysław, Angel, Emilio and Nico. It has really been a collaborative

group, rich of new ideas and collaborations among us, making both, the group and the individuals stronger.

A special dedication to Noemí, for being alongside with me these years and for enjoying together the best experiences of this period.

Finally I have to thank my parents, the most important brick of the castle, for always believing in me and in my potentials. For doing all the possible efforts that brought me till this point in life, but mostly for being a great example of the pearson I want to be. *Grazie mille Beddi.*

Abstract

During the last decade new technologies for the acquisition of 3D images have shown an impressive growth. One of these techniques that is worth mentioning, due to its capability of capturing the 3D information in a single shot, is known under different names such as *Integral Imaging*, *Plenoptic Imaging* and *Lightfield Imaging*. Since their invention at the beginning of the 20th Century but mainly after their rebirth in the '90s, lightfield imaging systems have gathered the attention of a vast community of researchers thanks to their promising capabilities of capturing 3D structure of incoherently illuminated scenes with just a single shot. These results are achievable thanks to the capability of these systems to capture not only the spatial information of the light rays emitted by the scene, but also its angular information. This has opened new research paths towards the design of improved systems, new dedicated algorithms, and a great amount of new applications, that can vary from phone cameras for bokeh effect, till cinema production for after effects. Lately, Integral-Imaging systems have shown very promising capabilities of capturing the 3D structure of microscopic samples. Nevertheless, there are some technical limitations inherent to this technology that needs to be taken into account.

In this Thesis we will analyse the theoretical principles of lightfield microscopy with particular focus to its bottleneck limitations with the scope of implementing new design solutions in order to overcome those problems. The aim of this work is to provide an optimal

design for 3D-integral microscopy with extended depth of field and enhanced lateral resolution. The principal focus of this Thesis has been to contribute making a step forward to the lightfield microscopy technique, in both directions: optical optimization of the capturing system and development of new algorithms for the reconstruction of the 3D sample.

Resumen

En las últimas décadas, ha habido un desarrollo notable de nuevas tecnologías de captura de imágenes 3D. Entre estas tecnologías existe una que merece una atención especial, por su capacidad de capturar la información 3D de escenas iluminadas incoherentemente. Esta técnica es conocida bajo varios nombres, según el área de conocimiento en que se investiga; *Imagen Integral*, *Imagen Plenoptica* y como es más conocida en ámbito internacional *Lightfield Imaging*. Desde su invención a principios del siglo XX, y más fundamentalmente desde su renacimiento en los años 90, está tecnología a captado una atención creciente en la comunidad científica debido a su capacidad para reconstruir escenas 3D a partir de una sola captura. Esta capacidad resulta de su habilidad para capturar en una sola toma, no sólo la información espacial de los rayos emitidos por los puntos que componen la escena, sino también la información angular. Esto, abre el camino hacia nuevos posibles escenarios de investigación y desarrollo no solo del sistema óptico, sino que también de todo el apartado de procesamiento de la información adquirida con algoritmos de reconstrucción más avanzados. Destaca también el interés en muchas aplicaciones que al día de hoy varían desde cámaras de telefonía móvil, para obtener mapas de distancia que permiten, entre otros efectos, el denominado efecto bokeh, hasta la producción cinematográfica de películas. Más recientemente se ha demostrado que los sistemas de imagen integral están en condiciones de proporcionar resultados muy interesantes también en el campo de la microscopía óptica. Sin em-

bargo, esta aplicación todavía presenta limitaciones técnicas inherentes a la misma naturaleza de la tecnología de imagen integral.

En esta tesis analizaremos los principios teóricos de sistemas de imagen integral para microscopía, con particular atención a sus limitaciones, con el objetivo de promover soluciones que puedan mejorar esos aspectos. Por esto, el enfoque principal de la tesis ha sido avanzar en la tecnología de microscopía de imagen integral en dos aspectos: en el desarrollo óptimo del sistema óptico de captura y en desarrollo de nuevos algoritmos de reconstrucción de la imagen 3D.

Resumen extendido

En las últimas décadas, el crecimiento exponencial en el desarrollo los componentes y tecnologías opto-electrónicas ha llevado al nacimiento y consolidación de la fotografía computacional. Dentro de esta línea de investigación son especialmente interesantes los sistemas de captura 3D de imagen integral. De hecho, el nacimiento de la imagen integral es muy anterior al de la fotografía computacional. Sin embargo, las limitaciones tecnológicas de la época impidieron su consolidación. Sin embargo, en las dos últimas décadas, ha vuelto a captar la atención de muchos laboratorios de investigación y empresas emergentes. De hecho, el interés internacional para estas tecnológica ha crecido tanto que se han presentado una notable cantidad de artículos en revistas y conferencias dedicadas a la representación 3D. No habrá que sorprenderse si la década actual será masivamente influenciada por nuevas tecnologías de entretenimiento 3D. Hay que destacar que la técnica de imagen integral es tan flexibles en sus aplicaciones que hasta el mundo de la microscopía 3D ha empezado a adaptar alguno de los sistemas pensados inicialmente para la captura de escenas 3D macroscópicas. Por estas razones, los objetivos de Tesis se han centrado en la adaptación de los principios de la imagen integral a la microscopía, con el propósito generar un avance en el conocimiento teórico, en el desarrollo experimental de la tecnología y en la implementación de un prototipo de microscopio integral de altas prestaciones. La Tesis está organizada en seis capítulos. El Capítulo 1 comienza con breve resumen histórico de los sistemas de obtención y

reproducción de imágenes 3D, continuando con la motivación de los objetivos del trabajo. En ese contexto se señala que, todos los sistemas fotográficos antecedentes han sido desarrollados para capturar una proyección 2D de un mundo 3D. Esto se ha conseguido tanto para escenas estáticas como para secuencias dinámicas. A partir de estos estímulos 2D, nuestro cerebro, que es un sistema altamente entrenado, es capaz de interpretar el espacio volumétrico de esas escenas gracias a algunas pistas fácilmente reconocibles en las imágenes: tamaño de los objetos, sombras y oclusiones. Aun así nuestro sistema visual necesita más pistas para inducir el cerebro a interpretar la información como un volumen 3D. Por ello, cuando se quiere desarrollar una nueva tecnología de imagen 3D no podemos olvidarnos de estimular todos los indicios visuales. Esos son de carácter psicofísico y físico. En el primer grupo caben las oclusiones, la perspectiva cónica, las sombras y el paralaje; en el segundo, por ejemplo, hay la acomodación, la convergencia y la disparidad. Sistemas de reproducción 2D pueden estimular fácilmente los indicios visuales psicofísicos, pero no llegan a la estimulación de los indicios físicos, y sin ellos nuestro cerebro no consigue una percepción del volumen como tal. Para suprimir a esta necesidad han sido desarrollados, por ejemplo, los sistemas estereoscópicos, que son capaces de estimular indicios de disparidad. Se habla de estereoscopia cuando un sistema permite la percepción de la profundidad a un observador binocular. Los sistemas convencionales de estereoscopía operan con dos imágenes que se presentan (de manera diferente según la tecnología utilizada) a los dos ojos del observador. Las imágenes reproducidas son capturadas desde dos perspectivas cercanas pero distintas. De esta manera se está proporcionando al observador una pareja de imágenes, que, a través del paralaje, estimulan su interpretación de volumen debido a la disparidad visual. Desde un punto de vista histórico se indica que ya en el siglo XIX, el científico británico Charles Wheatstone inventó el primer instrumento estereoscópico, el "Estereoscopio de espejo reflectante" diseñado con dos espejos a 45° respecto la línea de mirada del observador. Este dispositivo inspiró a muchas empresas fotográficas

a abrir una nueva dirección de producción de dispositivos comerciales de fotografía estereoscópica cuyo auge se ha alcanzado en el siglo XX. Nuevos dispositivos estereoscópicos seguían comercializándose con el intento de proporcionar una experiencia mejorada de la percepción 3D. Entre ellos se destacan los anaglifos, que alcanzaron una mayor difusión para la codificación/descodificación de estereogramas. Su principio está basado en la codificación en canales de color complementarios, como los colores rojo-cian, verde-magenta y azul-amarillo. Gracias a esta codificación, y al uso de gafas de anaglifo codificadas por colores, los ojos reciben dos imágenes separadas y es el cerebro el que las combina en una imagen estereoscópica. El mayor problema de esta tecnología es la limitación en la reproducción de colores fieles a la realidad. Más tarde se desarrollaron otras dos implementaciones basadas en el uso de gafas. La primera aprovechaba las propiedades de la polarización de la luz (gafas pasivas), así mediante el uso de filtros polarizadores, se proporciona a cada ojo su perspectiva correspondiente. La segunda implementación se basa en sistemas de gafas activas, capaces de binarizar la transmitancia de la lente (el sistema puede dejar que pase la luz o bloquearla), permitiendo en intervalos de tiempo sincronizados, la transmisión de las perspectivas a los respectivos ojos. Este proceso se repite secuencialmente, a una frecuencia superior a la crítica de fusión del sistema visual humano, para que los intervalos no sean percibidos y el observador consiga una percepción 3D. Ambos sistemas presentan ventajas e inconvenientes técnicos debidos a la tecnología adoptada, en el primer caso el filtro polarizador, en algunas situaciones específicas no puede bloquear correctamente la imagen destinada al otro canal visual, lo que implica un solapamiento no deseado de información. Las gafas pasivas, sin embargo, presentan una ventaja muy importante, el precio muy reducido para su realización, ya que no requieren partes activas controladas por sistemas electrónicos, ni baterías. Además, para un uso prolongado las gafas activas, y su sistema parpadeante, pueden causar malestar en el observador. A pesar de los problemas técnicos, ambas implementaciones presentan dos problemas que están en la base de

la ineficiencia de esta tecnología para su implementación en sistemas comerciales para observadores múltiples. Uno procede del hecho de que tienen sólo una perspectiva real de reproducción de la escena. Esto quiere decir que aquel observador que no está en la posición adecuada respecto a la pantalla, percibirá una sensación muy artificial de la representación, una experiencia muy alejada de la percepción real. Una versión más avanzada se basa en dispositivos personales con displays de soporte frontal (head mounted displays HMD), por lo que cada observador estará exactamente en la posición de visualización adecuada. De todos modos, todas estas tecnologías presentan un segundo problema que puede causar un profundo malestar en el observador que por tiempo prolongado visualiza esas imágenes. Dado que están basados en la percepción de la profundidad a través de la disparidad entre parejas de imágenes, el cerebro recibirá dos indicios visuales distintos y contradictorios; por una parte, la disparidad incita al cerebro a focalizar los ejes visuales a una distancia próxima. Sin embargo, la acomodación ha de seguir focalizada a una distancia más lejana, donde se encuentra la pantalla estereoscópica. El conflicto entre convergencia y acomodación, cuando sucede de forma prolongada es inherente a estos dispositivos y es fuente habitual de disconfort y malestar visual. Entonces el verdadero desafío es desarrollar técnicas de imagen 3D que solucionen el conflicto convergencia-acomodación del observador. Entre las tecnologías que están destacando interés en este ámbito hay que mencionar los sistemas de imagen integral. Estos sistemas se están demostrando muy eficaces en la captura y muestreo de escenas 3D. Permiten capturar la información espacial y angular de la escena y luego reproducirla en dispositivos dedicados para la visión del usuario. Debido a las características de su diseño permiten estimular de manera más completa el sistema visual humano, solucionando el conflicto convergencia/acomodación de los sistemas estereoscópicos. Esto resulta en una percepción más completa del volumen que se quiere reproducir, y el usuario no sufre incomodidad visual. El creador de estos sistemas fue G. Lippmann en 1908, justo el mismo año en que obtenía el Premio Nobel de Física por su método de

reproducción fotográfica en color basado en el fenómeno de la interferencia. Su idea se basa en la captura de la escena 3D a través de una matriz de microlentes, y reconstruirla con el mismo dispositivo, intercambiando el sensor por la película revelada, y añadiendo una iluminación en sentido contrario. En este sistema, la película fotográfica registra diferentes imágenes 2D pequeñas, cada una con información de perspectiva diferente. Una mejora el diseño de Lippmann fue presentada por Coffey en 1936, introduciendo una lente de campo para que la escena sea conjugada con el plano de las microlentes. Estos sistemas, aunque prometían buenos resultados, no llegaron muy lejos por la inmadurez de la tecnología de registro disponible en aquella época, que no se adaptaba al doble proceso de captura/reproducción de la fotografía integral. Solo en los últimos años, y gracias al importante avance tecnológico en los sistemas opto-electrónicos de captura y en las capacidades de procesamiento de las imágenes, esta tecnología ha vuelto a dar resultados cada vez más prometedores. Un estudio importante presentado por Adelson y Bergen, en 1991, llevó a la formalización del concepto de función plenóptica, íntimamente ligada a la radiancia de los rayos luminosos, y por tanto a su información espacio-angular. El aspecto que más atrae de los sistemas de imagen integral, es su capacidad para capturar con una sola toma la información 3D. Este detalle abre muchas puertas para nuevas implementaciones y aplicaciones. Una de las cuales es la proyección de la escena 3D a través de una matriz de microlentes, que permite la percepción 3D del volumen, sin necesidad de gafas, y evitando el conflicto convergencia/acomodación. De notable importancia es el aplicabilidad de esta tecnología a la microscopía. La posibilidad de obtener un sistema capaz de capturar la información 3D en una sola toma, y con iluminación incoherente ha focalizado el interés de una buena parte de la comunidad de microscopistas. Esta implementación en su primer desarrollo ha sido llamada (en inglés) lightfield microscopy, o microscopía integral (iMic). Gracias a su rapidez en la captura de la información abre un mundo nuevo para la observación de muestras 3D en vivo. De hecho, la tecnología integral llega después de años

de desarrollo de técnicas de reconstrucción 3D en el campo de la microscopia. La novedad y la relevancia es que tiene algunas ventajas importantes respecto a las otras configuraciones. Una de ellas es que no necesita implementar procesos de barrido mecánico (de la muestra o de la fuente de iluminación), reduciendo los tiempos de adquisición y permitiendo capturas en vivo. Hay que mencionar que también la microscopía de holografía digital consigue capturar la información 3D sin necesidad de barrido, sin embargo tiene un inconveniente, que es la necesidad de iluminación coherente, que conlleva muchas dificultades técnicas. Por otro lado, la microscopía integral se basa en iluminación incoherente demostrando una importante ventaja a la hora de la implementación de un sistema de captura 3D más versátil. Por todas estas razones, los sistemas de microscopía integral prometen tener un impacto importante y positivo en la microscopía óptica 3D. Y esta es la motivación de esta Tesis, durante la cual, el intento principal ha sido el desarrollo de nuevas implementaciones de sistemas de microscopía integral. Este objetivo se ha alcanzado a través de diferentes caminos, desde la optimización del sistema de adquisición de las imágenes, hasta la implementación de diferentes algoritmos para optimizar la reconstrucción 3D de las muestras. A continuación el Capítulo 2 se dedica a la descripción del estado del arte de los sistemas de microscopía integral. Empezando con una reconstrucción histórica que a través de varias publicaciones científicas ha llevado a las diferentes implementaciones de dispositivos de microscopía integral. Se denotan también las ventajas de este sistema respecto a otros ya conocidos y ampliamente desarrollados en el ámbito de la microscopía. Para llegar a una profundización mayor de estos sistemas se presenta un resumen de los aspectos principales de un microscopio convencional, cuyos factores más importantes son la resolución espacial y la profundidad de campo. De esta manera se puede empezar a presentar el microscopio original de imagen integral (iMic), analizando sus aspectos y sus limitaciones, que en concreto son las resolución espacial y la profundidad de campo. A estas limitaciones, varios investigadores han dedicado sus esfuerzos para mejorar los re-

sultados a través de algoritmos de desconvolución. Para mejorar la profundidad de campo del iMic explicaremos una implementación con lente líquida, que permite aumentar notablemente la profundidad de campo, al coste de perder la capacidad de obtención de la información 3D en una singola toma. Finalmente pasando al Capítulo 3 será descrita una nueva implementación óptica de microscopio integral, conocida como microscopio integral en el dominio de Fourier (FiMic). La nueva configuración, que ve las microlentes desplazarse del plano imagen del microscopio (configuración iMic) al plano de Fourier del objetivo de microscopio (FiMic), será introducida en sus principios teóricos, justificando el interés en implementar el nuevo diseño. El FiMic nos permitirá mejorar ambas limitaciones del clásico iMic; la resolución y la profundidad de campo, además de proporcionar un sistema mucho más flexible y fácil de usar para el usuario. Los algoritmos de desconvolución de las imágenes obtenidas para el clásico iMic, siguen siendo válidos para las nuevas capturas, esto quiere decir que las mejoras pueden afectar tanto el sistema óptico como los algoritmos ya publicados. A lo largo del Capítulo 3 serán presentadas las características de diseño del FiMic. Esto nos permitirá entender sus ventajas frente al iMic, y además aprender cómo configurar los diferentes elementos ópticos del diseño, y adaptarlo a las necesidades requeridas para las distintas muestras, variando resolución y profundidad de campo solo con modificar el tamaño de las microlentes elegidas. A conclusión se añadirá la descripción de una implementación experimental enfocada en la comparación con resultados entre FiMic e iMic. Seguiremos con el Capítulo 4 que ha sido dedicado a los algoritmos de reconstrucción de la información capturada a través de un FiMic. El desarrollo de algoritmos de reconstrucción es tan importante como la implementación óptima del sistema óptico de captura de la imagen integral. Estas dos vías no pueden ir disjuntas, sino que tienen que complementarse en el intento de sacar el máximo provecho posible de estos sistemas. Sin embargo, hasta la fecha, los sistemas lightfield han conocido una gran expansión en el ámbito de la fotografía macroscópica. Eso implica que para esos

sistemas se ha alcanzado un avance muy importante y notable no sólo en los sistemas ópticos de captura, sino que también en los algoritmos de reconstrucción de las escenas 3D. Se podría pensar que como el sistema de formación de imagen fue adaptado de manera bastante sencilla a los microscopios, de la misma manera se podrían utilizar los algoritmos ya publicados para sistemas macroscópicos, en sistemas de microscopía. Desafortunadamente, la solución no es tan inmediata, debido a diferencias esenciales de los objetos que los dos sistemas capturan. Fijémonos en que el mundo real microscópico es muy rico en texturas colores y formas conocidas, mientras que en microscopía las muestras presentan más limitaciones en esos aspectos, siendo a menudo dispersas, con fondo oscuro o plano, con poca riqueza de colores y con una mayor densidad de oclusiones. Todo esto hace más difícil el desarrollo de algoritmos para la microscopía integral. Por esto, no hay una solución óptima para todas las posibles muestras, sino que hay que adaptar el algoritmo para que sea versátil en función de las posibles características singulares de cada muestra. Todos estos aspectos han sido detallados en el Capítulo 4, junto con varias implementaciones que se proponen para solucionar situaciones específicas de diferentes muestras. Los algoritmos desarrollado han sido cuatro en total. Tres de ellos dedicados a muestras dispersas, cada uno optimizado para diferentes situaciones y requisitos de la muestra y del usuario, como la posibilidad de resolver oclusiones o la rapidez y el seccionado óptico del segundo, o incluso la mejora de la resolución. El último algoritmo ha sido diseñado para ser el más completo de todos, ya que permite variar muchos parámetros de configuración, haciéndolo adaptable a la mayor cantidad de tipologías de las muestras. En el Capítulo 5 presentamos una aplicación para el FiMic que hemos desarrollado con el afán de extender su rango de aplicaciones. Por esto, si hasta aquí se habían tratado sistemas de microscopía con iluminación convencional de campo claro y de fluorescencia, hemos decidido añadir una configuración más, basada en iluminación de campo oscuro. Esta técnica de iluminación, ya muy conocida y utilizada por muchos microscopistas, permite la vi-

sualización de muestras transparentes, o puras de fase. Con esto añadimos un apartado muy interesante e importante para aquellos microscopistas que trabajan en esta configuración, ya que ahora se permitirá la captura de información 3D de esas muestras. Terminamos con el Capítulo 6 donde se resumen los resultados obtenidos y se delimitan posibles áreas de investigación futura, mayormente enfocadas en algoritmos de reconstrucción de las capturas obtenidas, posiblemente con algoritmos de inteligencia artificial, capaces de alcanzar resultados óptimos en tiempo real.

Acronyms

2D	Two-dimensional
3D	Three-dimensional
HVS	Human visual system
IP	Integral photography
InIm	Integral imaging
MLA	Microlens array
iMic	Integral microscope
FiMic	Fourier integral microscope
DOF	Depth of field
FOV	Field of view
MO	Microscope objective
WD	Working distance
TL	Tube lens
AS	Aperture stop
NA	Numerical aperture
ORP	Object reference plane
BFP	Back focal plane
LL	Liquid lens
EI	Elemental image
FS	Field stop
RL	Relay lens
S&S	Shift and sum
S&M	Shift and multiply
MIP	Maximum intensity projection

OS	Optical sectioning
SNR	Signal to noise ratio

Contents

Chapter 1

Introduction

In the past two decades the exponential growth in optoelectronic technologies and components has brought up a new trend for photography: the computational photography. Thanks to that, some old proposals, that were kept in the drawer due to inadequate resources disposable by that time, are now being exploited and are becoming the center of attention of many research laboratories and industrial parties. Until recent years, most of the progress was centered in capturing 2D representations of the 3D world. This was done through either static photography or dynamic video. With these inputs, our brain, which is a very well trained system, is able to understand the volumetric space of those images or videos thanks to some cues inherent to the real world, such as image dimensions and occlusions. But even if looking at an image that we are able to process somehow, our brain still lacks some additional cues in order to really perceive that information as a volume. It is a fact well known that for the human visual system (HVS) there are many cues that induce our brain to interpret the world around us as 3D. So in order to develop a 3D technology we need it to be able to stimulate our HVS in the proper way, introducing some psychophysical and physical cues. Occlusions, conical perspective, shadows and movement parallax are just some examples of psychophysical cues. Physical cues are accommoda-

tion, convergence and disparity. Whilst normal 2D systems can easily tackle psychophysical cues in such a way that we are able to interpret 2D images as representation of the 3D world, what they lack are the physical cues. Without them we are unable to properly perceive the scene as 3D. To fulfill this need to stimulate physical cues in the proper way, new technologies are in constant development. Based on the concept of the binocular nature of the HVS, stereoscopic systems have been built and studied. The idea is to shoot a couple of pictures of the same scene with two cameras that are separated horizontally by a certain distance, and to show later, simultaneously, each of the two images to the corresponding eye of the observer. In this way a binocular disparity is provided to the HVS and consequently also convergence is stimulated, inducing the observer's brain to be tricked and to elaborate the information as depth perception of the scene. The first stereoscope was proposed in 1838 by Wheatstone [1]. Few years later, Rollman proposed to use complementary colors to codify the stereoscopic pairs, and then he reported the use of anaglyphs [2]. It became a very popular method, but not for long, because of the poor capacity of color reproduction. This kind of technology is experiencing a new growing interest due to its easy application and due to the improvements in the quality of the imaging system. The color coding has been changed for polarisation coding [3,4] overcoming the problem of poor color reproduction. However even if stereoscopic systems have dramatically improved, they still lack some physical cues. As a matter of fact, the stereo-pair images provided to our eyes, stimulate the convergence in order to trigger the brain to interpret the 3D scene. This cue works in direct competition with other cues which are not triggered, or even worse give a different depth cue to our brain, like accomodation that suggests a flat interpretation in the case of a stereo-pair. The result is that most people can watch stereo videos, but not for too long, because they experience vision fatigue, nausea and other discomforts. Auto-stereoscopic displays give the user a stereoscopic pair, but without the need of wearing special glasses. They use lenticular sheet [5] or parallel barriers [6]. Even

if not wearing glasses reduces the discomfort, this solutions do not overcome the so called "convergence-accommodation" conflict. The real challenge is to provide both convergence and accommodation cues to our brain. To this aim, real 3D displays have been developed, which does not need the use of dedicated glasses or the aid of an auto-stereoscopic device. Among these implementations volumetric displays [7,8] and holographic displays [9] have shown promising results, since they can provide 3D experience and avoid vision fatigue. However, the implementation of holographic displays, still presents technical difficulties due to inadequate technology (i.e. sufficiently small and bright pixels). A different concept, originally presented in 1908 by Lippmann, was named as integral photography (IP). In [10] he described a system where a microlens array (MLA) is placed in front of a photographic film. This device permitted to capture several images of the same scene, each with a different perspective of it. Once the scene is captured, the idea of Lippman was to use those captured images to display the scene allowing 3D perception. The system anyway showed some problems due to the overlapping of the elemental images behind each microlens, and a depth field limited to objects close to the camera. An improvement of the Lippmann's concept was proposed by Coffey [11], who introduced a field lens that formed the image of the scene onto the MLA. This design was later refined by Davies et al. [12], but, due to the poor instrumentation of that time, the technology has been hibernated until recent years, when it has come back thanks to improvements of the optoelectronic technology in terms of imaging quality and of processing capability. With the new reborn interest toward this technology, some authors called it integral imaging (InIm) [13,14]. Since then, many interesting applications have been proposed, such as the capture and display of integral images [15,16], and a multi-camera array system for the capture of InIm [17]. An important study was done in 1991 by Adelson and Bergen who formalised the concept of plenoptic function, the radiance of any luminous ray, holding spatio-angular information [18]. Based on the concept of plenoptic function many experiments have been

carried out and also commercial cameras have been released [19–21], converging on the name of lightfield imaging because the aim of such systems is to capture and represent the lightfield of the 3D world. Nowadays many applications use and take advantage of the lightfield technology [14, 22–30]. One of the most attractive and direct applications is the projection of the scene through a monitor with a matrix of microlenses in front of it, allowing for the perception of 3D without the need of wearing any glasses [5, 15, 31]. Apart from this, it must be noticed that the capability of obtaining a 3D reconstruction of the scene with a single shot is of great interest among many research fields. Recently, lightfield technology has experienced a fast growth in the research community, but interestingly it has been applied also to offer solutions to a variety of problems in the biomedical sphere such as: otoscopy [32], ophthalmology [33], endoscopy [34,35], and for static [36, 37] or dynamic [38–40] deep-tissue inspection. Lightfield systems have been adapted for wavefront sensing [41], 3D imaging using long-wave infrared light [42,43], head-mounted display technology [44,45], or large 3D screens [46,47]. The applications of lightfield imaging are expanding very quickly and reaching also very differentiated kinds of applications, such as gigapixel photography [48], 3D polariscopy [49], the inspection of road surfaces [50], or the monitoring of the red coral [51]. The advantage is to be able to reconstruct the 3D scene with just one single shot [13, 52–56], obtaining a volumetric reconstruction of it [57–59]. The capacity of capturing 3D information with a single shot and with incoherent illumination has triggered the attention of the microscopist community. This application, has been called lightfield microscopy, and also integral microscopy (iMic). The idea of being able to acquire the 3D image of microscopic samples with just one shot is really intriguing for many research areas [60], because it allows for in-vivo imaging of 3D specimens. As a matter of fact lightfield microscopy has come after a long tradition of 3D reconstruction technologies in microscopy. The novelty, though, is that with respect to previous techniques it does not need a scanning process like the scanning of the sample or of the illumination

beam, which implies long process for one acquisition and possible errors due to sample vibration during the mechanical displacement. This is the major drawback of most other techniques when applied to live-samples. Nevertheless, there are other techniques capable of obtaining the 3D information with just one single shot. Among them, digital holographic microscopy [61,62], allows to capture a hologram of the sample and extract from it, through computation, the complex amplitude of the sample at different depth planes. The main inconvenience of this technique is the need of coherent illumination, which implies several technical difficulties. On the other hand, lightfield microscopy does not need a dedicated coherent illumination, it allows to take the 3D information of a sample with incoherent illumination and just one shot.

For all the above mentioned arguments, lightfield microscopy has the potential of making an important contribution to 3D microscopy. This is the motivation of this Thesis, in which the principal intent has been to develop lightfield imaging systems for microscopic samples. This scope can be reached by different means, from the design of an optimized acquisition system, till the image analysis and reconstruction of samples through dedicated algorithms. In order to do so, the first step has been the study of the state of the art of lightfield microscopy. This allowed to gain a deep insight into the advantages and disadvantages of the lightfield microscopes developed, is strongly required in order to be able to make step forwards in this growing field. All these aspects will be explained and detailed along the chapters of this Thesis and our proposed solutions will be given. Apart from theoptical design, also pros and cons of the state-of-art algorithms for the 3D reconstruction of the sample will be analysed. Also in this case, some improvements will be proposed for optimized reconstruction of the acquired information.

The mentioned objectives will be presented and explained in the following way. In Chapter 2 theoretical fundamentals of lightfield microscopy will be given together with the analysis of some limitation of the system, whose improvement will be detailed in the following

Chapters. In Chapter 3 a new design for lightfield microscopy will be presented, showing among other benefits, better lateral resolution and depth of field. Chapter 4 is dedicated to the reconstruction algorithms. Due to sample variety, different approaches have been studied in order to achieve the best possible performances in each case. The following Chapter 5 presents a particular application of the FiMic for the case of transparent samples, where an adjustment of the illumination beam (dark field illumination) allowed us to capture the 3D structure of pure phase objects, and recontruct its volume thanks to one of the algorithms described in Chapter 4. Finally, in the last Chapter 6 some final remarks will be underlined with the aim of summarizing the presented work, and presenting ideas for future works.

Chapter 2

State of art

There are some branches of research in microscopy that concentrate
their efforts in the study of biomedical processes that requires 3D live
imaging acquisition. Therefore, for them it is necessary to obtain,
rapidly, stacks of images in depth. This would allow the inspection
of the dynamic of some biological functions, and the response of bio-
logical systems to external perturbations. Currently, most of the 3D
techniques are based on confocal microscopy [63–67], structured illu-
mination microscopy [68–70], or light-sheet microscopy [71,72]. Each
of them has a specific task where it is more efficient than the other
techniques, but what they have in common is the need of multiple
shots in order to capture the 3D volume. To perform these shots,
some mechanical scanning is required, it can be either scanning of
the sample or of the illumination beam that could have detrimen-
tal effects if mechanical vibration or timing are an issue. A solu-
tion, that avoids mechanical movements, is digital holographic mi-
croscopy [73–75]. The main drawback of holography is that it is
based on the recording of interference patterns, which requires co-
herent illumination. This, has substantially two disadvantages: it is
very sensitive to imperfections and it makes fluorescent imaging im-
possible. Recently, the proposal of using an electrically-tunable lens
allowed a scanning process without mechanical movements [76–79].

However, while solving mechanical problems it introduces aberration issues that must be taken into account. An interesting technique for capturing the 3D volume with a single shot is the plenoptic or lightfield microscopy. This technique is based on the capture of multiple perspectives in a single shot. Then, 3D volume is computationally extracted from the multi-perspective information. This is possible because objects at different depths present a parallax offset between perspectives. Lightfield microscopy is adapted from the lightfield camera used in the macroscopic scale. With respect to the lightfield cameras, which have the drawback of capturing views with low parallax for far scenes, the lightfield microscope has the advantage that the scene (or 3D sample in this case) is so close the first lens (microscopic objective) that the admitted angles are much bigger and thus, parallax is high. The first attempt to adapt the lightfield concept to microscopy was reported by Jang and Javidi [80]. In their work, they used a microlens array in order to display the 3D structure of a microscopic sample. At that time, the integral image, used for the reconstruction, was obtained indirectly from a stack of 2D images of the sample captured through a confocal microscope. In 2006 Levoy et al. [60], reported a microscope design in which a MLA was placed at the image plane. It was named as the lightfield microscope. With the captured integral image, that contains the spatio-angular information of the 3D scene, it was possible to apply new algorithms to extract further informations such as the depth refocusing and the extraction of multiple perspectives of the sample. Their work is nowadays considered as a fundamental reference in the lightfield microscopy community. From that work, many research groups started to contribute to the growth of this new technology, trying to improve some of its limitations such as poor resolution and depth of field. Many solutions along the years have been proposed, some based on time or space multiplexing [81, 82], and others on computational interpolation or deconvolution [83, 84]. A newer approach uses a relay system for enlarging the exit pupil of the microscope objective and to fit in it an array of cameras [85]. It is composed of 25 CCTV lenses placed

close to the enlarged exit pupil and capturing the perspective views which are later processed. All these processes have a strong drawback in the heaviness of the data processing required, having the paradoxical effect of disabling real-time applications. Note that immediacy was the main reason for using lightfield technologies in microscopy. A design solution that does not involve big computational time, was proposed and named as Fourier Integral Microscopy (FiMic) [86,87]. Its name comes from the fact that the MLA is not placed at the image plane as in a normal iMic, but at the Fourier plane of the microscope objective. FiMic will be the principal system solution adapted for the development of this Thesis, its design parameters as well as algorithms and applications will be described. As it will be discussed in detail along the Thesis, FiMic has the advantage of providing better resolution and depth of field (DOF) than an iMic, as well as projecting a direct image (multi-perspective) of the sample onto the sensor, this will help the microscopist to move the object into the desired position.

2.1 Conventional Microscopes

Before analyzing in depth the characteristics of lightfield microscopes, let us begin with a general description of the conventional-microscopy scheme. This will help us to introduce the tradeoffs intrinsic of the lightfield microscopes and therefore to deeper understand certain design specifications. A microscope is an optical instrument capable of making images of small objects, whose smallest features cannot be distinguished from direct sight or using a single magnifier. In general, all the microscopes, from the simplest to the most sophisticated, have one common component, the microscope objective (MO). It plays a very important role determining the quality of the image through essential parameters like spatial resolution, aberrations, contrast, DOF and field of view (FOV). Depending on the position of the object plane, there are two classes of MOs, one corrected to a finite distance, and the other corrected to infinity. The MOs of the first class
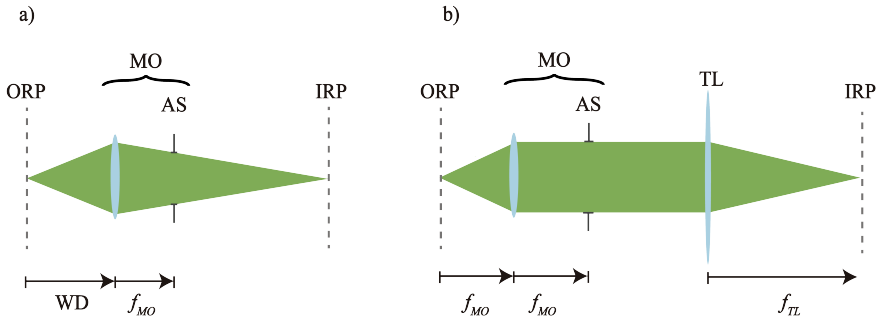
a)   b)

Figure 2.1: Schematic of a microscope working with a finite distance (a) and another corrected to infinity (b).

are designed in such a way that they provide the aberration-corrected image at a finite distance. In this case the distance, so-called working distance (WD), from the object plane to the objective is larger than the focal length of the MO, see Fig. 2.1(a). On the contrary, the infinity corrected MOs are designed so that the object plane is just at the front focal plane. This produces the aberration-corrected image at the infinity. Therefore, an additional lens, called tube lens (TL), is needed to focus the final image at a finite distance, see Fig. 2.1(b).

In the infinity-corrected MOs the aperture stop (AS) is often set at the back focal plane of the MO. This defines the most important characteristic of a MO, its numerical aperture (NA). The numerical aperture expresses the capability of the MO of collecting the incoming light, and is defined as:

$$NA = n\,sin(\alpha) \tag{2.1}$$

being n the refractive index between the sample and the MO and α is the semi-aperture angle as measured from the axial point of the object plane (see Fig. 2.2.).

From now on we will consider only microscopes equipped with infinity-corrected MO, and therefore the schematic of a conventional microscope will be the one of Fig. 2.3, composed by a MO, a tube
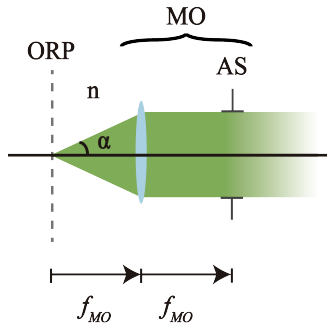
Figure 2.2: Example of the definition of the Numerical Aperture (NA) of a microscopy objective.

lens and an imaging sensor.

2.1.1   Lateral resolution of a conventional microscope

In many optical instruments the effects produced by the wave nature of light are not appreciable, and therefore those systems can be studied and modelized in terms of Geometrical Optics, allowing to represent their behaviour through ray diagrams. Applying this assumption to image-forming instruments, the image of the object results to be an exact replica of it, scaled with the lateral magnification of the system. In these cases, the limit to the lateral resolution is simply determined by the size of the pixels of the sensor. This is not the case in microscopy where the size of the features under observation objects is of the order of the wavelength of the illumination beam. In this situation it is not possible, anymore, to simply study the system through ray diagrams, but diffraction effects must be taken into account. Let us consider a 2D object of amplitude transmittance $u_0(x, y)$ that is illuminated, under normal incidence, by a monochromatic plane wave. Following the Fresnel-Kirchhoff diffraction theory it is easy to obtain the amplitude distribution on the image plane, Fig. 2.4(a), of the microscope as [88]:
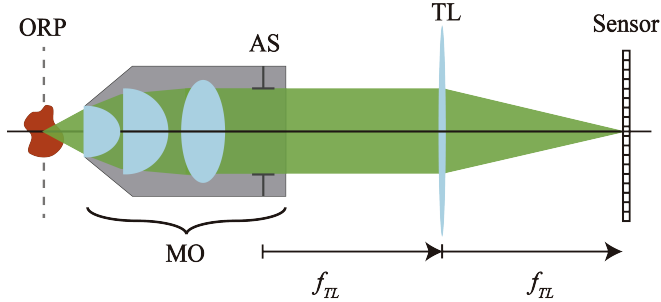
Figure 2.3: Schematic of a conventional microscope as will be considered throughout the thesys. Its principal elements: the microscopy objective (MO); the tube lens (TL); the imaging sensor. Furthermore, we can see in the schematic the object reference plane (ORP) and the aperture stop (AS).

$$u_1(x,y) = \frac{1}{M} u_0 \left(\frac{x}{M}, \frac{y}{M} \right) \otimes_2 \tilde{p} \left(\frac{x}{\lambda f_{TL}}, \frac{y}{\lambda f_{TL}} \right) \tag{2.2}$$

In Eq.(2.2) the symbol $\otimes$ represents the 2D convolution product, the symbol $\sim$ identifies the Fourier transform of the function under it, $M = -f_{TL}/f_{MO}$ is the lateral magnification of the microscope and $p(x,y)$ is the pupil function of the MO, meaning the transmittance of the AS. Usually, the AS is a circular aperture of radius r_p, and therefore its Fourier transform gives an Airy-disk function:

$$\tilde{p} \left(\frac{r}{\lambda f_{TL}} \right) = Disk \left(\frac{r}{\lambda f_{TL}/r_p} \right) \tag{2.3}$$

Following Eqs.(2.2) and (2.3), it is evident that, if diffraction effects are considered, a point object will be imaged as an Airy disk, as shown in Fig. 2.4. The resolution limit is usually expressed as the radius of the first ring of the Airy disk, whose value is

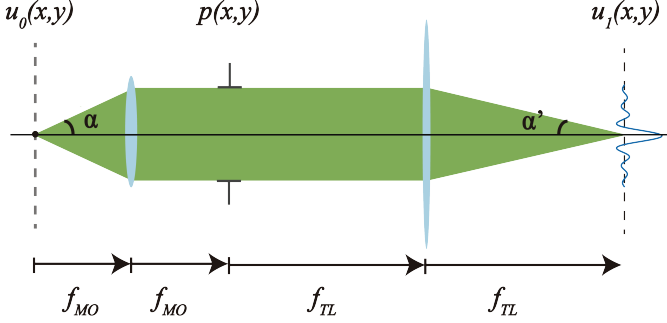$$r_0' = \frac{0.61\lambda f_{TL}}{r_p} \tag{2.4}$$

Figure 2.4: Drawing of the impulse response of a conventional microscope, from the object plane $u_0(x, y)$ till the image plane $u_1(x, y)$.

This equation can be rewritten as a function of the NA, but evaluated at the image space, $NA' = n' sin(\alpha')$. Taking into account that α' is a small angle, then we can apply the paraxial approximation, $NA' \simeq r_p / f_{TL}$, and therefore $r'_0 = 0.61\lambda / NA'$. The size of the Airy disk is considered to be the minimum distance between two distinguishable point sources, in other words, the resolution limit of the system. As formulated by Lord Rayleigh, two Airy disks are resolved if their distance is bigger than r'_0, therefore the resolution limit can be expressed in the image space as:

$$\rho'_R = \frac{0.61\lambda}{NA'} \tag{2.5}$$

It is more intuitive to define this limit in the object space, in order to know exactly what can be resolved

$$\rho_R = \frac{0.61\lambda}{NA} \tag{2.6}$$

Naturally, this value is related to M, the lateral magnification of the system, and $\rho'_R = M\rho_R$. Another way of defining the resolution limit is the E. Abbe formula, that takes into account the cut-off frequency of the MO, and evaluates the resolution limit as:

$$\rho_A = \frac{\lambda}{2\,NA} \tag{2.7}$$

No matter which equation is used to calculate the resolution, the important principle is that both are inversely proportional to NA. Thus, the bigger NA, the smaller the resolution limit, and consequently the higher the resolution power achieved.

2.2 Plenoptic microscopes

As exposed above, the first application of Lippmann's IP concept, adapted for capturing multiple perspectives of 3D samples with a single shot, was made by Levoy [60], who named the technique as lightfield microscopy. This name has been very controversial due to the fact that the term lightfield is very general and can describe many techniques in which a wave, or a ray, or a field of light is used. For this reason, in the years after such report, other names were proposed, like plenoptic microscopy of integral microscopy (iMic). Although it seems that in the past two or three years the name lightfield microscopy is prevailing over the other denominations, along this manuscript we will use instinctively any of the three denominations. In its simplest design, an iMic is composed by a MO, a tube lens, an array of microlenses and an imaging sensor. As shown in Fig. 2.5 the MLA is placed at the image plane, and the sensor is displaced to the back focal plane of the lenslets. In this way, the rays emitted by (or passing through) the sample at the object reference plane (ORP), which coincides with the MO front focal plane, are focused on the MLA. The role of the microlenses is to collect the light rays passing through their centers. Those rays will impinge onto the sensor, which is placed at the back focal plane (BFP) of the MLA. The portion of the capture behind each microlens will be called here as microimage. Note that the microimages contain the radiance map of the specimen, meaning its spatial and angular information.
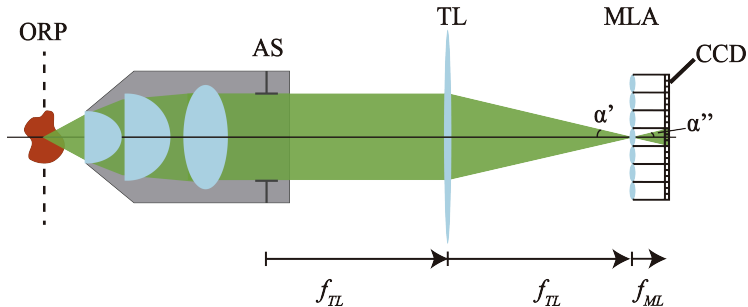
Figure 2.5: Schematic of an integral microscope (iMic), composed from left to right of a: microscope objective (MO); tube lens (TL); microlens array (MLA); imaging sensor (CCD).

2.2.1 Radiance map captured with a lightfield microscope

According to the scheme shown in Fig. 2.5, we can state that the primary role of the coupling formed by the MO and the TL is to provide a highly magnified image of ORP onto the MLA. It is also of great importance the fact that the MO and the TL are coupled in afocal manner, and that the AS is placed just at the common focal plane. This implies that both the entrance and the exit pupil are located at the infinity, making the system fully telecentric. The light cones, emerging from each point of the object, are symmetric and with constant angular width in both the object and the image spaces, as shown in Fig. 2.6(a). In this way the radiance distribution on the plane of the MLA (x_0, θ_0) can be represented with the spatio-angular diagram of Fig. 2.6(b). Note that we assume the approximation that only rays passing through the center of the lenslets are considered. Also, we assume the approximation of considering only the rays impinging the center of the pixels. In a conventional telecentric microscope, moving the sample laterally will not produce any parallax [60]. This is not the case in an iMic, which registers the plenoptic function, because the MLA allows the capture of the angu-
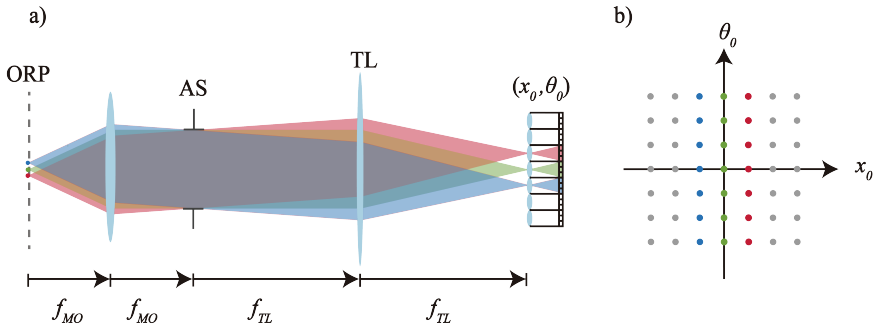
Figure 2.6: a) Rays from the ORP till the sensor of a system telecentric in the object and image space. b) representation in the spatio-angular diagram of the plenoptic function of an iMic.

lar information of the rays emitted by the object. Considering that in iMic all the optical elements are placed with an afocal configuration, the lateral magnification will be constant and will not dependend on the depth. Therefore, the extracted images are orthographic views of the sample.

2.2.2 Relationship between objective and microlenses NAs

The relationship between the NA of the objective and that of the microlenses is important to be analysed because it determines the behaviour of the system and its performances. The NAs play an important role, defining the size of the light cone impinging the sensor behind each microlens. That size must be carefully thought and designed in order to take optimal advantage of the pixels in the sensor and at the same time, to avoid any crosstalk between microimages. From Fig. 2.5 it is easy to notice that both the angles α' and α'' must be equal. In other words, the numerical aperture in the image space of the microscope $NA' = NA/M$ must be equal to that of the microlenses NA_{ML}. Assuming that paraxial approximation holds in the image side of the microlenes, this can be expressed as:
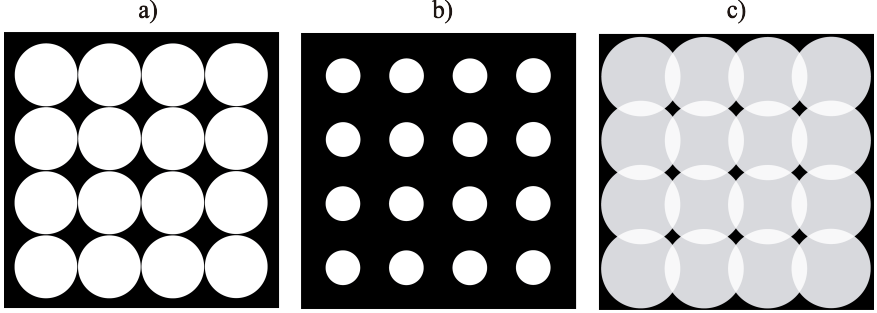
Figure 2.7: Microimages captured in the following cases: a) $NA' = NA_{MLA}$; b) $NA' < NA_{MLA}$; c) $NA' > NA_{MLA}$.

$$\frac{NA}{M} = \frac{p}{2\,f_{ML}} \qquad (2.8)$$

where p, the pitch, is the distance between microlenses, and f_{ML} is their focal length. Examples of different NAs are shown in Fig. 2.7. If Eq.(2.8) is respected, then, the use of the pixels is optimal and crosstalk is avoided.

2.2.3 Lateral resolution for iMic

When considering a conventional microscope, thought for observation of microscopic specimens, the lateral resolution is of key importance. If we neglect the diffraction effect, the lateral resolution is determined basically by the cut-off frequency of the CCD. Under the same assumption, in the case of the iMic the resolution limit would be determined by the pitch of the MLA, because it is the parameter that determines the sampling at the image plane, see Fig. 2.8. Following the Shannon's sampling theorem, two points are resolved if their images fall on two non adjacent microlenses. Taking into account the magnification of the system M, then the lateral resolution as evaluated in the object space is
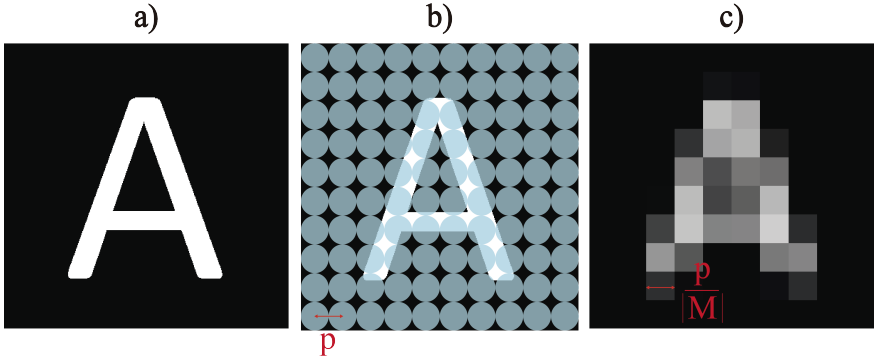
Figure 2.8: Spatial resolution of an iMic, the ORP (image a) is conjugated with the MLA plane (image b). The pitch p is the distance between the centers of two microlenses, in this way the pitch divided by the absolute value of the lateral magnification of the system (| M |) will determine the size of the equivalent pixel in the object space, resulting in an image like c).

$$\rho_{views} = \frac{2p}{M} \tag{2.9}$$

This resolution limit is referred to the simple capture of the iMic, but the actual lateral resolution achievable at different depths after the reconstruction is different. Since the reconstruction is obtained interlacing the pixels of different orthographic views, it has been demonstrated that the lateral resolution obtained in the reconstruction is contained in a certain interval [89]:

$$\rho_{rec} = \left[\frac{p}{M}, \frac{2p}{M} \right] \tag{2.10}$$

Since the resolution limit is proportional to the pitch of the lenlets, one could think that the resolution can be improved at will by reducing the pitch of the MLA. Nevertheless, one factor that can never be underestimated in microscopy is the diffraction, and the smaller the microlenses the more diffraction affects the capture. Meaning that, if the microlenses are not sufficiently large with respect to the Airy Disk

given by the microscope, it will not be possible to assume that the system works in parageometical approximation and the assumptions made earlier will not be valid anymore. This condition can be expressed as $p = \mu\rho'_R$ being μ a real number. Even though there is not a mathematical verification for a minimum value of μ, it has been experimentally proven, and widely accepted, that a good advice is that the dimension of the lenses should be at least four times greater than the Airy disk of the system ($\mu \geq 4$). This assumption worsen the resolution of the equivalent conventional microscope system by a factor 2μ.

More generically, considering also wave-optics the formula of the resolution will be:

$$\rho_{view} \geq max \left\{ \frac{\lambda}{2\,NA}, \frac{2p}{M} \right\} = \mu\frac{\lambda}{NA} \qquad (2.11)$$

This means that iMic sacrifices significantly lateral resolution in order to capture the angular information needed for the 3D reconstruction.

2.2.4 Depth of Field of an iMic

In conventional microscopy, and assuming that pixels are small enough, it is well known that the resolution is strictly related to the numerical aperture of the microscope objective as Eqs.(2.6) and (2.7) show, but another important factor that is affected by the NA is the depth of field (DOF). Its expression for a conventional microscope is

$$DOF^{conv} = \frac{\lambda}{NA^2} + \frac{\Delta x}{M\,NA} \qquad (2.12)$$

being Δx the pixel size. The first term can be considered as the diffractive effect, and the second the geometrical contribution. This formula can be applied for the calculation of the DOF of the iMic system. In the iMic case, to estimate the value of the DOF for the computed views of the capture, one should take into account that the rays from one point object passing through the microlens will be further subdivided by the number of pixels behind a microlens

[60]. The last subdivision has the effect of increasing the DOF as it reduces the maximum incident angle of rays reaching the pixel. Since the Airy disk of the microscope will be μ-times smaller than the microlenses pitch p, that defines the angular resolution capability. It is good practice to choose a sensor with a number μ of pixels behind a microlens (in one direction) [60]. In that case the equivalent incident angle onto one of the pixels will be μ -times smaller, and therefore the geometrical contribution to the DOF μ-times greater following this equation:

$$DOF_{view}^{iMic} = \frac{\lambda}{NA^2} + \mu\frac{p}{M\,NA} \tag{2.13}$$

Taking into account the definition of parameter $\mu = p/(\frac{\lambda M}{2\,NA})$, this equation can be rewritten as:

$$DOF_{view}^{iMic} = \frac{\lambda}{2\,NA^2}(2 + \mu^2) \tag{2.14}$$

In conclusion the iMic is able to produce a collection of perspective images which, in the best possible realization, have a resolution that is 8 times worse (considering $\mu = 4$) than the one provided by the conventional microscope. If the resolution limit falls proportionally to the numerical aperture, the depth of field shortens proportionally to its squared value. If we consider that the interest of lightfield microscopy is to reconstruct 3D scenes, it is a drawback that the depth of field gets so narrow as those parts of the sample that does not fall within the DOF will not be properly reconstructed.

Enlargement of depth of field of an iMic

It is interesting now to evaluate the possibility of improving the DOF of an iMic in order to increase the thickness of the captured 3D volume. One solution is the insertion of a liquid lens (LL) in an adequate plane. The LL is a plano-convex lens whose curvature, and therefore its focal length, can be electrically tuned. This can help to improve
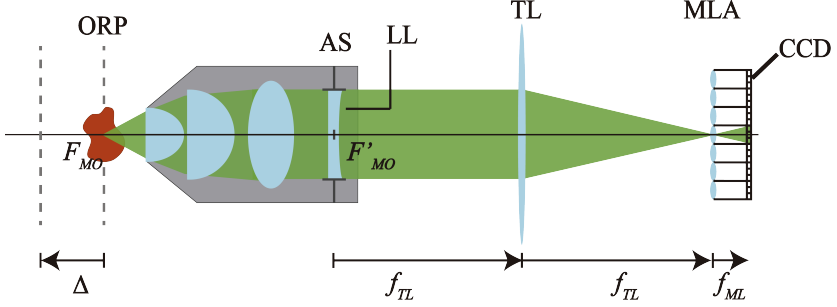
Figure 2.9: Schematic of the iMic modified by the insertion of a liquid lens at the AS of the MO. With this configuration, a displacement (Δ) of the object reference plan (ORP) is achieved as described by Eq.(2.15).

the DOF while keeping fixed other parameters such as FOV and resolution [76, 90, 91]. As shown in Fig. 2.9 the liquid lens is inserted at the AS of the MO. An easy explanation of the effect of inserting the LL can be derived by applying ABCD matrix formalism [92]. With this formalisme is straightforward to find that when a thin lens, in this case the LL, is inserted at the BFP of an MO, some parameters change, but some others remain unaltered. To be more specific, both the focal length and the position of the BFP remain unchanged. However, the FFP is displaced axially by the distance

$$\Delta = \frac{f_{MO}^2}{f_{LL}} = P_{LL}\, f_{MO}^2 \qquad (2.15)$$

Here $P_{LL} = 1/f_{LL}$ is the optical power of the LL. Depending on the fabrication parameters of the LL, its optical power can take positive and negative values, therefore the FFP can be shifted in both positive and negative directions. In other words, by simply tuning the voltage of the LL, one can shift at will, between certain limits, the position of the ORP, while keeping constant all the other parameters like resolution and magnification. It is straightforward to apply this design to a conventional iMic as shown in Fig. 2.9, with the aim of capturing a collection of lightfield images, each corresponding to a
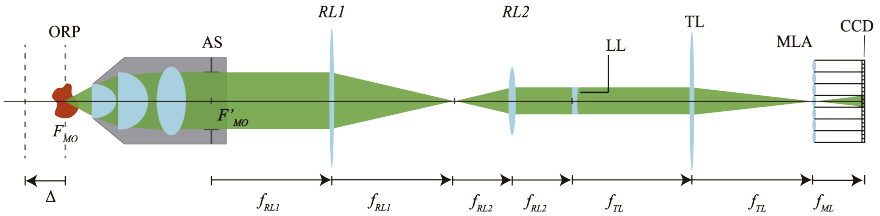
Figure 2.10: *Schematic of the iMic with the insertion of a LL coupled with a relay. We used a relay system composed by two lenses of focal lengths $f_{RL1} = 150mm$ and $f_{RL2} = 75mm$, respectively, and disposed in afocal configuration. The LL is then placed at the back focal plane of RL2 .*

different axial position of the ORP in order to extend the total depth of field of the final reconstruction as reported in the Article [II].

Experimental validation

To prove this idea we used the setup shown in Fig. 2.10. The implementation of the iMic was done with: a MO of 50x magnification and NA = 0.55; a tube lens with $f_{TL} = 100mm$; a MLA with pitch $p = 110\mu m$ and $NA_{ML} = 0.01$; and a LL with diameter $\Phi_{LL} = 3.5mm$ manufactured by Varioptic (ARCTIC 39N0). An additional relay, needed to couple the AS with the LL, was made with two lenses RL1 and RL2, with $f_{RL1} = 150mm$ and $f_{RL2} = 75mm$. The relay magnification, $M_R = f_{RL2}/f_{RL1} = 0.5$, allowed to match the AS diameter, $\Phi_{AS} = 7.2mm$, with the diameter of the LL. The LL used in the experiment is based on the electrowetting principle and it is made of two liquids with the same density but different refractive index. A voltage is applied to change the curvature. At room temperature it works in linear range and its power can be calculated by the following equation:

$$P_{LL}(T) = S(T)[V - V_0(T)] \tag{2.16}$$

where the temperature is expressed in Celsius and: $S(25) = 1.068(m \cdot V)^{-1}$ and $V_0(25) = 41.1V$. The insertion of the relay system slightly
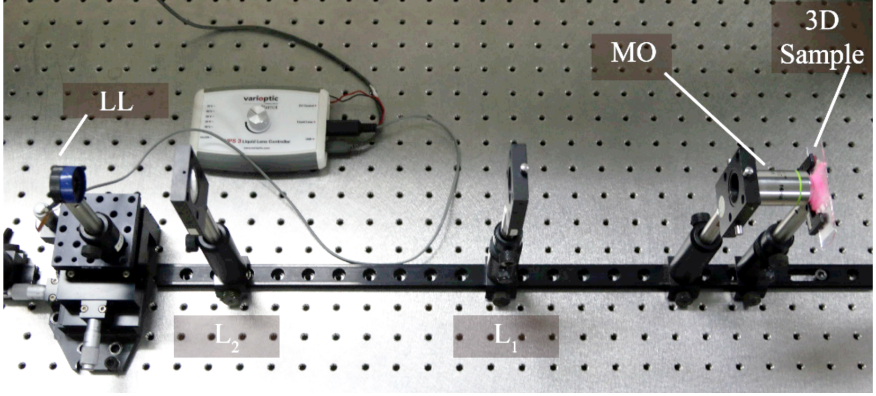
Figure 2.11: Details of the experimental setup

modifies the results expressed in Eq.(2.15), since now the axial magnification of the relay M_R^2 must be considered:

$$\Delta^{eff} = P_{LL}\, M_R^2\, f_{MO}^2 \qquad (2.17)$$

Fig. 2.11 shows a picture of the experimental setup, from the sam-

$V(V)$	$P_{LL}(m^{-1})$	$\Delta^{eff}(\mu m)$
38	-3.3	-13.2
40.1	-1.1	-4.3
42.2	1.2	4.7
44.3	3.4	13.7
46.4	5.7	22.6
48.5	7.9	31.6
50.6	10.1	40.6
52.7	12.4	49.6
54.8	14.6	58.5
56.9	16.9	67.5

Table 2.1: Optical power induced to the LL and the effective displacement of the ORP obtained changing the applied voltage
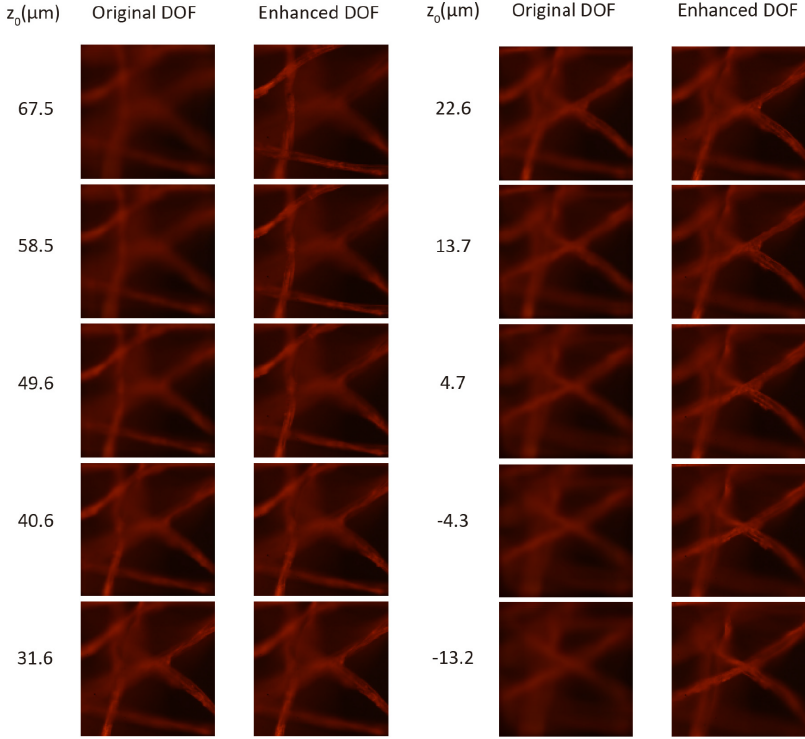
Figure 2.12: Comparison of the depth reconstruction with the conventional method (left column) and with the proposed method (right column)

ple to the LL. In our experiment we captured a total of 10 lightfield images, each after the ORP. The voltage applied was changed from 38.0V to 56.9V as shown in Table 2.1 together with the Δ^{eff} obtained. In each step the displacement is of $9\mu m$ and it corresponds to DOF/2. To compare the new results with a conventional capture we reconstructed the captured sample (cotton fibers stained with fluorescent dye) in two ways: in the first one we reconstructed the volume with just one of the captures (V=48.5V), that more or less corresponds to the central zone (in depth) of the sample; and the sec-
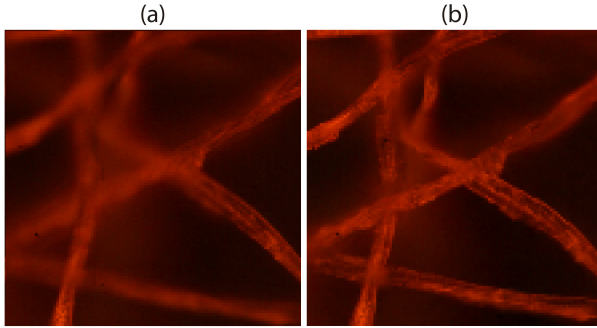
Figure 2.13: DOF comparison of perspective views obtained with (a) conventional iMic, and (b) proposed method of iMic coupled with a LL

ond one was obtained stacking together the reconstructions computed with the ten captures. Fig. 2.12 illustrate the two reconstructions and it is clear that, thanks to the multi-depth captures, the fibers are resolved along all the volume of the sample, which spans from $-13.2\mu m$ till $67.5\mu m$, with a total volume of $80.7\mu m$ in depth . From the left columns it is clear that the conventional iMic is limited to a narrow DOF, which, in this case is around $17\mu m$. Another way of comparing the whole DOF for the two cases is to show the perspective views in both cases as in Fig. 2.13. Fig. 2.13(a) shows the central view of the conventional iMic, and Fig. 2.13(b) is obtained with the registration of all the captures, where the DOF is clearly increased.

Chapter 3

Lightfield Microscope with capture in Fourier Domain

Until here the conventional configuration of the lightfield microscope has been described and analysed. It has been demonstrated that, with the information acquired, it is possible to computationally reconstruct the 3D volume of the sample under inspection. Nevertheless, two drawbacks have been reported: its low resolution and its limited depth of field. Both of them represent the biggest brake to the growth of this technology. Given the optical limitations of iMic, some effort has been put in trying to overcome these lacks by computational methods. This is the case of some non-conventional deconvolution procedures, like those reported by Broxton et al. [83] or by Stefanoiu et al. [93]. However, although those algorithms provide reconstructions with some improvement in contrast, they have the drawback of strongly increase the computation time, and, of course, of not being able to recover the information of an object that is not captured optically. Thus, although we do not deny the utility of such kind of computational procedures, we think that the primary effort should be put in improving the optical system in order to capture the biggest amount of 3D information. Naturally, computational tools are welcome after better images are captured. In this Chapter
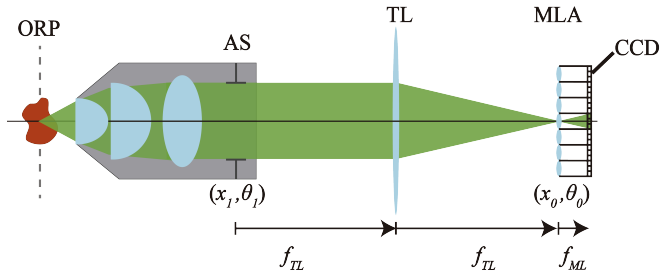
Figure 3.1: Schematic of an iMic. Through the transfer matrix A of the system it is possible to obtain the relation between the coordinates of the plenoptic function between the two planes (x_0, θ_0) and (x_1, θ_1).

we show that with some simple, but essential, design modifications of the conventional lightfield microscope (iMic), significant improvements, in terms of resolution and DOF, of the captured perspective views are achieved. The proposed design is the result of a change of paradigme. Instead of placing the microlenses at the image plane of the microscope, we propose to place them at the Fourier plane of the microscope [86, 87, 94]. Note that it is really a change of paradigm since the Fourier plane is at the far field (i.e. the infinity) of the image plane. Taking this into account it is reasonable to name this new microscope as the Fourier integral microscope (FiMic).

3.1 FiMic design configuration

Let us consider a conventional lightfield microscope as in Fig. 3.1. It is interesting to analyse the radiance distribution at the AS plane and at the microlenses plane. Making use of the ABCD formalisme, the relation between the spatio-angular information at these two planes can be calculated easily

$$\begin{pmatrix} x_1 \\ \theta_1 \end{pmatrix} = A^{-1} \begin{pmatrix} x_0 \\ \theta_0 \end{pmatrix} \tag{3.1}$$
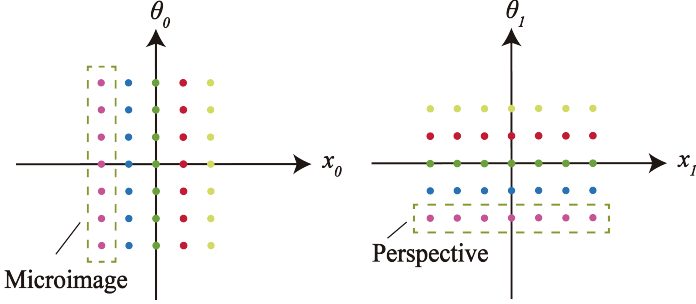
Figure 3.2: Spatio-angular diagram of the MLA plane a) and of the plane of the AS b) in iMic.

with

$$A = \begin{pmatrix} 1 & -f_{TL} \\ 0 & 1 \end{pmatrix} \begin{pmatrix} 1 & 0 \\ 1/f_{TL} & 1 \end{pmatrix} \begin{pmatrix} 1 & -f_{TL} \\ 0 & 1 \end{pmatrix} = \begin{pmatrix} 0 & -f_{TL} \\ 1/f_{TL} & 0 \end{pmatrix}. \tag{3.2}$$

Then

$$\begin{pmatrix} x_1 \\ \theta_1 \end{pmatrix} = \begin{pmatrix} 0 & f_{TL} \\ -1/f_{TL} & 0 \end{pmatrix} \begin{pmatrix} x_0 \\ \theta_0 \end{pmatrix}. \tag{3.3}$$

This equation shows clearly that the spatio-angular information of the lightfield suffers basically a transposition when propagating from the AS to the MLA. This is illustrated with colors in Fig. 3.2. In other words, it suggests that if the iMic configuration has Q microlenses and T pixels per microlens, we could collect the same spatio-angular information by placing T microlenses at the AS with Q pixels behind each microlens. This transposition implies that there is another way of building a lightfield microscope, placing the microlenses at the aperture stop. With this new configuration, considering the spatio-angular transposition, it is apparent that each microlens will capture an orthographic image (spatial information). The angular information is collected through the different orthographic images, each with a different perspective, provided by the microlenses.
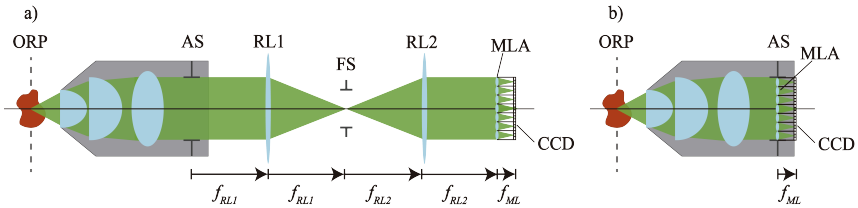
Figure 3.3: (a) Schematic layout of the Fourier Integral Microscope (FiMic). From left to right the object reference plane (ORP), the microscope objective and its AS, the two relay lenses RL1 and RL2, the field stop FS, the microlens array (MLA) and the imaging sensor (CCD); (b) Same principle but much more compact realization

3.1.1 Implementation of a Fourier integral microscope (FiMic)

In practice, placing a microlens array (with T microlenses) at the aperture stop and a sensor behind it gives the same result of placing an equivalent number T of micro-cameras in the AS. Unfortunately, in the market there are no such small cameras, therefore, a microlens array and a coupled sensor will be used instead for the development of this Thesis. Another practical problem that must be taken into account is that most of the telecentric objectives have their aperture stop inside their body, which makes it impossible to physically place the MLA where it should be. An optical solution is given by the use of an afocal relay system, which conjugate the Fourier plane and the MLA plane. A second reason why it is worth to add an afocal relay is to make the design much more flexible for the implementation of different experimental configurations (as will be discussed in the next Sections).

The fact that in FiMic the MLA is conjugated with the AS allows the microlenses to spatially multiplex the aperture stop. The portion of the sensor behind one microlens will directly capture an orthographic image of the sample, called here as elemental image (EI). This means that each EI contains the spatial sampling of the specimen, the
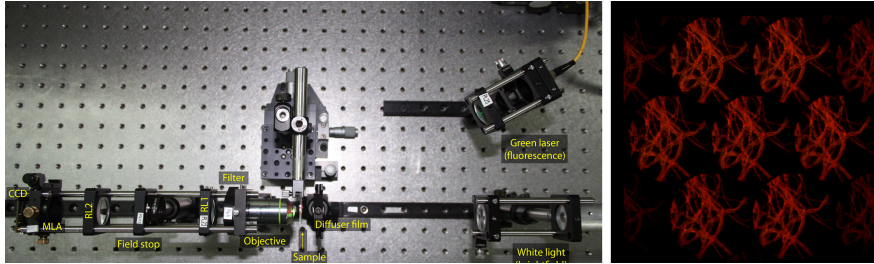
Figure 3.4: The setup used for the acquisition, with the fluorescence laser used to illuminate the samples, and a sample output image acquired. On the right side the seven elemental images are visible.

angular information, instead, is obtained thanks to the effect of multiplexing the aperture stop. Now, points of the object with the same lateral position, but at different depths, will appear separated (i.e. with disparity) in the EIs. In Fig. 3.3(a) we show the scheme of the experimental setup used in Article [I] in order to study the behaviour of FiMic. The optical components needed to implement an FiMic are the following: the microscope objective (MO), two converging lenses (RL1 and RL2) for the relay system, the field-stop (FS), the microlens array (MLA), and the CCD. In a fully custom design, the number of elements needed to build an FiMic would be just three: the MO, the MLA and the CCD (Fig. 3.3(b)). In that case it will be necessary, as well, to have full control over the illumination beam and its NA in order to avoid crosstalk between EIs. This setup would be really compact, but it would lack compatibility and versatility. Therefore for the scope of this Thesis, as well as for a more complete analysis of the performances of the FiMic, the less compact design was built and studied, as shown in Fig. 3.4. Note that it is necessary to put the MLA accurately onto the AS, otherwise there would be a significant loss of information in the outermost EIs. The field stop is placed in between RL1 and RL2, at their common focal plane, so that its image is projected at the BFP of each microlens. The size of that image determines the size of the EIs and helps to avoid two unde-

sired situations: the first one is optical crosstalk between EIs when the image of the FS is too big (see Fig. 3.5(b)); and the second one is the unnecessary waste of pixels when that image is too small (see Fig. 3.5(c)). In an optimal implementation (see Fig. 3.5(a)), the size of the image of the FS must be equal to the pitch p of the MLA, and it is determined by the magnification, $M_{FS} = f_{ML}/f_{RL2}$. According to this, the diameter of the FS must be:

$$\Phi_{FS} = \frac{p}{M_{FS}} \tag{3.4}$$

The field stop, as the name itself suggests, has an impact on the field of view (FOV) of the FiMic

$$FOV = \Phi_{FS} \frac{f_{MO}}{f_{RL1}}. \tag{3.5}$$

As mentioned above each MLA multiplexes the light information impinging the AS, this implies that each EI provides a different angular sample of the same spatial information. This new way of sampling the AS indicates that there is another important thing that must be carefully treated when capturing brightfield images: the illumination beam, which must meet some criteria (usually omitted in the discussion regarding the design of a lightfield microscope). The lightfield microscope collects both the spatial and the angular information of the lightfield emitted by the sample. If one does not want to contaminate this information with the illumination beam, it should be spatially and angularly uniform. In practice this means that the FOV must be uniformly illuminated and the illumination beam must have a numerical aperture that matches that of the MO, in this way the AS will be uniformly illuminated and the MLA can perform properly its function. This precautions avoid the undesired effects of vignetting in the aperture stop, which would cause different illumination intensity within and between the EIs.
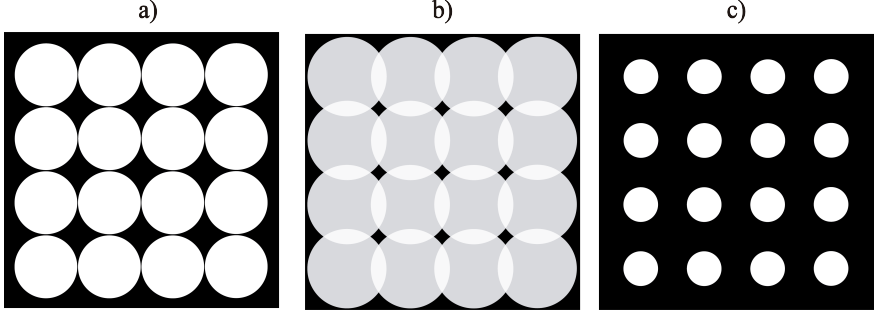
Figure 3.5: Different sizing of the FS affects the optical barriers: a) optimal situation with tangent EIs; b) undesired situation with FS too big means a waste of pixels in the crosstalk areas.; c) undesired situation with FS too small also means a waste of pixels in the black areas.

3.1.2   The FiMic feature parameters

We start this section by recognizing that the, real or virtual, insertion of the MLA at the AS, will affect the performances of the original microscope. To analyse the first implication of the MLA, let us consider the Fig. 3.3 and remind the each lenslet is providing an orthographic EI of the specimen, but using only a portion of the aperture of the MO. The consequence is that any EI is obtained with an effective numerical aperture that is a fraction of the original NA. Considering the formula of the numerical aperture:

$$NA \simeq \frac{\Phi_{AS}}{2\,f_{MO}} \tag{3.6}$$

Assuming that along the AS diameter we fit N microlenses, then, the effective NA

$$NA_{eff} \simeq \frac{1}{N}\,\frac{\Phi_{AS}}{2\,f_{MO}} \tag{3.7}$$

or simply

$$NA_{eff} = \frac{NA}{N} \tag{3.8}$$

where N can be calculated as

$$N = \frac{\Phi_{AS}}{p'} \tag{3.9}$$

being $p' = p\,\frac{f_1}{f_2}$ the pitch as evaluated at the aperture plane. Naturally, any change in the effective NA has a direct influence in the performance parameters of the microscope, like the resolution limit or the DOF. Concerning the resolution limit, there are two factors that must be taken into account, the diffraction effects and the finite size of the sensor pixels. Considering first wave-optics, the resolution limit is

$$\rho_{Airy} = \frac{\lambda}{2\,NA_{eff}} = N\frac{\lambda}{2\,NA}. \tag{3.10}$$

In order to take into account the influence of the pixels we must remind that two points are resolved if they are imaged on different pixels, but leaving at least an empty pixel between them, therefore if the size of the pixel is δ, then

$$\rho_{geom} = 2\delta\,\frac{f_{RL2}\,f_{MO}}{f_{RL1}\,f_{ML}}. \tag{3.11}$$

When the system is not perfectly balanced the actual resolution is given by the maximum value between them:

$$\rho_{FiMic} = max\left\{ N\frac{\lambda}{2\,NA}, 2\delta\,\frac{f_{RL2}\,f_{MO}}{f_{RL1}\,f_{ML}} \right\}. \tag{3.12}$$

An optimal situation is actually when the two terms for this formula are equal. This can be achieved by choosing the optimum pixel size:

$$\delta = N\,\frac{\lambda}{4\,NA}\,\frac{f_{RL1}\,f_{ML}}{f_{RL2}\,f_{MO}}. \tag{3.13}$$

Regarding the DOF we can calculate it adapting the classical formula to the effective NA_{eff} of the FiMic:

$$DOF_{FiMic} = \lambda \, \frac{N^2}{NA^2} + \delta \, \frac{N}{NA^2} \, \frac{f_{RL2} \, f_{MO}}{f_{RL1} \, f_{ML}}. \qquad (3.14)$$

If we now substitute the optimum value of δ in Eq.(3.14) the formula simplifies to:

$$DOF_{FiMic} = \frac{5}{4} \, \frac{\lambda}{NA^2} \, N^2. \qquad (3.15)$$

3.1.3 The FiMic vs. the iMic

In order to have clear the advantages of FiMic, we focus this section in the comparison of the performances of both systems in terms of resolution and depth of field. Both microscopes are designed to capture the radiance distribution, i.e. the spatial and angular information of the specimen. The different positioning of the MLA along the two systems makes the difference of the information captured at the sensor plane. In fact, in iMic the microlenses spatially sample the object and the pixels behind any microlens capture the angular information of the corresponding point. On the contrary, in FiMic the microlenses make the angular sampling and the sensor behind them make the spatial sampling. By comparing the resolution and DOF formulae derived in Sections 2.2.4 and 3.1.2 we find the following relations

$$\rho_{EI} = \frac{N}{2\mu} \rho_{view} \quad \text{and} \quad DOF_{EI} = \frac{5 \, N^2}{4 + 2\mu^2} DOF_{view}. \qquad (3.16)$$

Given a specific iMic; that is, given a value of μ (always bigger than 4.0), different values of N can be chosen so that the FiMic has much better resolution but equivalent DOF, or much higher DOF but equivalent resolution. Other intermediate values of N provide some trade-off with an improved resolution and DOF. These improvements are obtained by FiMic at the cost of lowering the density of the angular
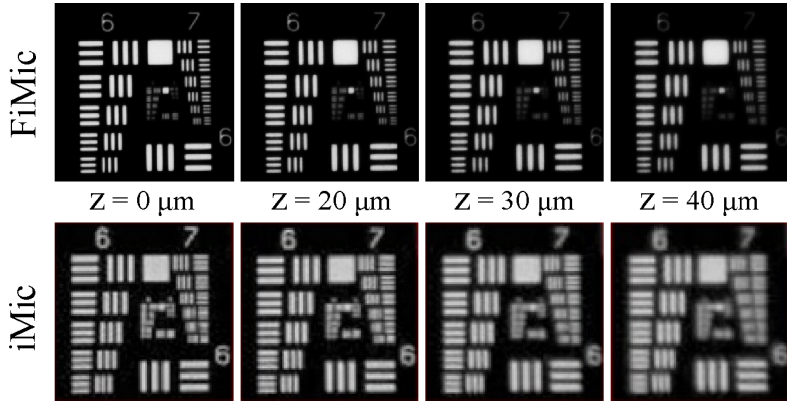
Figure 3.6: Central view provided by both microscoper when operating with the same DOF. The FiMic provides better resolution at the edge of its DOF than the iMic at its ORP

sampling, which is not a big cost, because the redundant information is already sufficient for the application of the reconstruction algorithms, which will be treated in the next Chapter. To validate the theoretical derivations, we have designed an experiment that permits the analysis of two different cases. Since FiMic has a much more flexible design, we chose to implement an iMic whose parameters are fixed: lateral resolution of $6.2\mu m$ and $80\mu m$ DOF.

a) FiMic with better resolution than iMic but equivalent DOF

The optical elements of the FiMic were chosen in order to provide a DOF of $80\mu m$, and are the following. An infinity corrected MO with magnification 20x, and therefore $f = 10.0mm$, $NA = 0.5$ and $\Phi_{AS} = 10.0mm$. The relay system was formed by two achromatic doublets with $f_{RL1} = 200mm$ and $f_{RL2} = 100mm$. We used an MLA with $f_{ML} = 6.5mm$, $p = 1.0mm$, and $NA_{ML} = 0.077$ (APH-Q-P1000-R2.95 manufactured by AMUS). Finally the sensor was a CMOS camera (EO-5012c 1/2") with 2560x1920 square pixels of $\delta = 2.2\mu m$
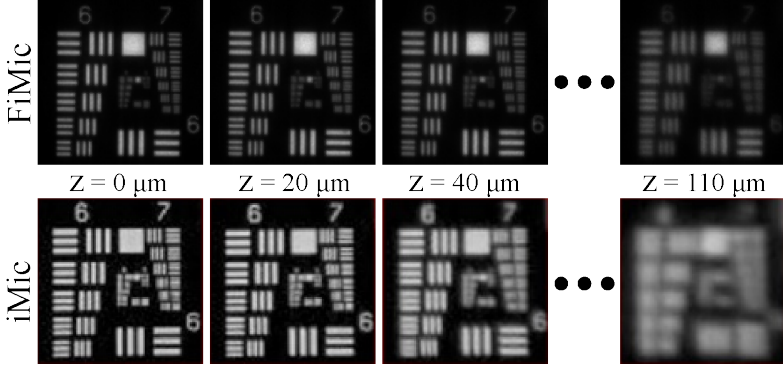
Figure 3.7: Central view provided by both microscoper when operating at resolution limit of about 6.2μm. The label Z indicates the distance from the ROP, the DOF extends up to Z = +110μm fot the FiMic, but only up to Z = +40μm for the iMic.

in side. With these optical elements we got a value of $N = 5.0$, which gives a $DOF = 77\mu m$ and an expected resolution limit of $3.4\mu m$. In order to evaluate the resolution we used an USAF resolution chart. In the first step it was placed at the object reference plane. After each capture, with the help of a micrometer, it was axially displaced of a constant step, up to the limits of the DOF. The central views of both lightfield microscopes (EIs for FiMic, and computed views for iMic) are shown Fig. 3.6. Note that only positive axial displacements are shown, but for negative displacements it gives the same results. The resolution measured in the case of FiMic is of $3.9\mu m$, better than the $6.2\mu m$ of iMic, and it is maintained better than the one of iMic along all the DOF. It is noticeable that FiMic provides better resolution at the edge of the DOF than iMic at the ORP.

b) FiMic with longer DOF than iMic but equivalent resolution

In this case we used the same MLA as before, but a different MO ($f = 9.0mm, NA = 0.4, \Phi_{AS} = 7.1mm$) and relay system ($f_{RL1} =$

$f_{RL2} = 50mm$). In this case $N = 7.1$ and therefore the lateral resolution limit is $6.1\mu m$ and the DOF is of $240\mu m$. As in the precedent case, the plenoptic images of a USAF were obtained with the two lightfield microscopes. Again the central views, for different axial positions of the USAF target, are shown in Fig. 3.7. In both configurations, the best resolution obtained, at $z = 0\mu m$, is the element 3 of group 7 of the chart, which corresponds to a resolution of $6.2\mu m$. Considering the limit of the depth of field as the plane where the resolution decreases by a factor $1/\sqrt{2}$, the limit will be achieved when the least element recognisable is the element 6 of group 6 ($8.76\mu m$). This value must be multiplied by two because also negative depths will behave in the same way. With this experiment we found a DOF for iMic of $80\mu m$ and for FiMic of $220\mu m$, which corresponds to an improvement of 2.75 times, which for a 3D volumetric specimen is an important achievement.

Chapter 4

Reconstruccion techniques for lightfield microscopes

With this Chapter we start the analysis focusing on how to proceed, by computational method, in order to take advantage of the spatio-angular information acquired. In this sense, along the development of this Thesis different techniques and approaches have been proposed. Before even starting the discussion, it must be pointed out that there is not such thing as the perfect algorithm for all the samples, since image analysis has strong dependence on the type of sample. This is the reason why different approaches have been investigated in order to try to fulfill the different possible situations most common in microscopy. Macroscopic lightfield imaging is already, indeed, a very hot topic among the researchers and industries, with many algorithms developed for a very broad types of scenarios, able to provide very fine depth estimation. When those techniques are directly applied to lightfield microscopy, results do not have high accuracy because of the nature of such images. Microscopic biological samples do not present a wide and sharp range of colors like most of macroscopic scenes. Instead, they are often semi-transparent or sparse samples in a fluid. Under these conditions, conventional algorithms result in noisy reconstruction depth-maps. This is the reason why a more ro-

bust approach is needed in order to exploit the information captured by the lightfield microscopes.

4.1 Depth from defocus

The easiest way to obtain a 3D reconstruction from the captured lightfield image is a technique mostly known as the *refocusing algorithm*, but it would be more precise to call it selective defocusing, since it allows to use the captured lightfield to calculate depth images in which one plane appears sharp (i.e., in focus) and the other planes appear with increasing blur (or defocus). In other words, from a collection of EIs that have sharp images along the DOF, the refocusing algorithms permits to select, at will, which depth must be kept sharp while blurring the others. As an example this could be applied in what today is a really hot-topic for mobile phones: the bokeh effect in a selfie with post processing. Going back to microscopy it can be interesting to be able to select a depth within a sample and see what is in focus there, because it means the user can identify parts of a sample at a specific axial position. Many algorithms have been proposed for lightfield refocusing [13, 19, 58, 95–98], each having a slight different nature, but providing comparable outputs: the objects at a selected depth appear sharp whilst other depths appear defocused. This is why, with the aim of providing a general refocusing tool we introduce here the easiest one. This algorithm is broadly called Shift and Sum (S&S), and, as its name suggests, it consists in shifting the elemental images towards a central one, and summing (and normalising) their intensity at each step of the shift. After each step the result is stored in a stack of images called focal stack. What happens is easy to understand if we remember that in lightfield technologies, different depths correspond to proportional parallax (or disparity) changes in the images. Let us consider the example proposed in Fig. 4.1(a) where three circular objects emit light of different wavelength. The green circle is at the ORP, the red one behind it and the blue one in front of it. The three circles are perfectly aligned with the optical
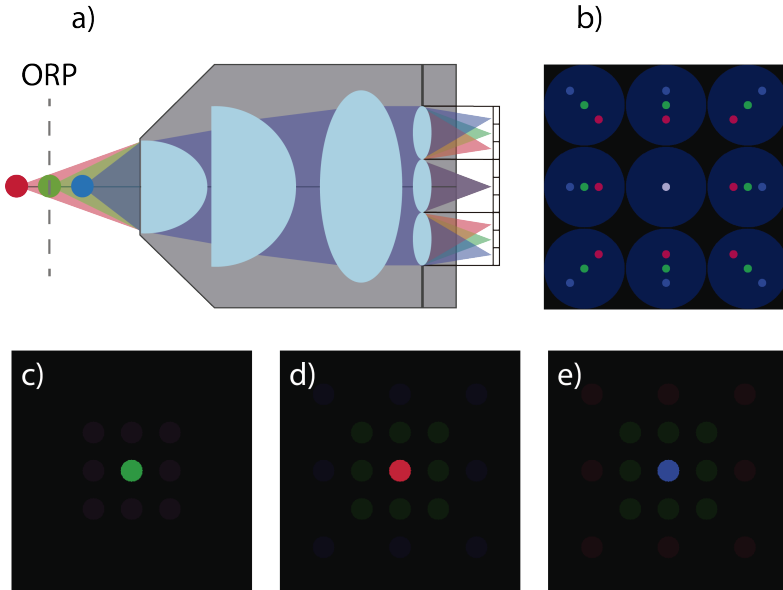
Figure 4.1: a) compact FiMic schematic with three circles in the optical axes at different depths; b) simulated capture of 9 EIs showing how the disparity changes as a function of the depth; c) d) e) in order show the green circle at the ORP, the plane of the red circle behind it and the plane of the blue circle in front of it.

axis and therefore their image onto the central EI, Fig. 4.1 (b), will overlap. If we have a look at the central EI, the three colors sum creating a white circle, while in the other EIs, only the green circle (that lays on the ORP) is perfectly centered. The other two circles positioned at different depths (positive for the red and negative for the blue) are captured with disparity in the external EIs.

Summarizing, what lays on the ORP is imaged on the EIs with no disparity, whilst objects behind or in front of that plane will present some disparity. If now we think of superimposing all the EIs, one on top of the other, summing the correspective pixels and normalising them, it is evident that only those objects captured at the ORP

will perfectly fit one on top of the other, whilst the other objects will not exactly coincide with their replicas. This means that after summing in this way all the images, only the objects at the ORP will appear sharp and the other blurred, as shown in Fig. 4.1(c). If now we introduce an extra shifting factor as Fig. 4.1(d) and (e)), objects at the ORP will appear blurred and the objects with a determined depth (related to that shifting factor) will now appear sharp. To generate the whole focal stack, this procedure is repeated for all the shifting factors needed to cover the whole DOF. Once the focal stack is computed, with the help of a maximum intensity projection (MIP) algorithm the 3D volume can be represented in a virtual space in the monitor of the user. For the calculation of the focal stack we need to introduce a new parameter Δz that is the smallest possible step in depth achievable and it can be calculated as in Article [I]:

$$\Delta z = \frac{f_{RL2}^2 \, f_{MO}^2}{f_{RL1}^2 \, f_{ML}} \frac{\delta}{p}.$$

(4.1)

While Δz is the smallest step, the refocusing depth, i.e. the axial coordinate of the refocused plane, is a function of the disparity (or shift) value d applied at each step of the focal stack generation:

$$Z_{obj} = -d \, \Delta z.$$

(4.2)

Here d can take positive and negative values. When the EIs are perfectly superimposed one on top of the other $d = 0$, which corresponds to the ORP, whilst positive values of d means negative Z_{obj} and vice versa. Obviously, Z_{obj} is measured from the ORP. This algorithm is very easy to implement, however it has the drawback that the scene information coming from out-of-focus objects is present at each slice of the focal stack, resulting in a disturbingly noisy background when the 3D volume is displayed. To overcome this issue, other algorithms have been developed in this Thesis.
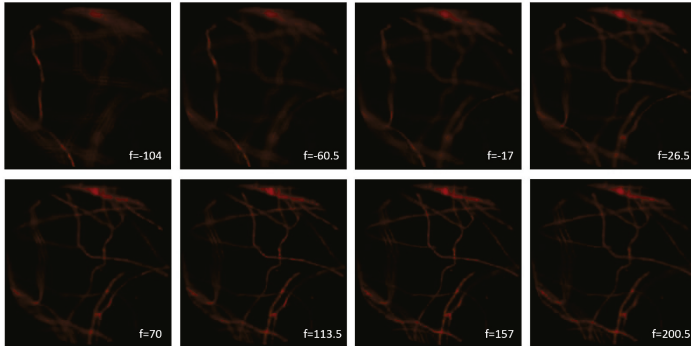
Figure 4.2: Examples of the refocused images extracted from the focal stack generated by shift and sum algorithm. Unit of length: μm

4.2 Area-based depth estimation for monochromatic feature-sparse orthographic capture

Our first approach [99] was proposed for the case of fluorescent sparse samples, a situation that is actually very common in microscopy. When a specimen is stained with a fluorescent dye, only certain specific cells or organoids, involved in the metabolism of that fluorophore, will emit light at a predetermined wavelength. Therefore, is of actual interest to have an algorithm capable of providing a 3D reconstruction in these cases. The proposal is to use the depth from defocus (DFF), that estimates depth of 3D scenes from a focal stack [74, 100, 101]. Conventional DFF algorithms were originally developed for obtaining a depth map from a stack of 2D images, captured with a conventional camera, focused at different depths and with very narrow DOF. A "*focus*" measure that evaluates the sharpness of an object is used in sub-regions of the whole image in order to determine its depth from the stack. This measure outputs a maximum value when the object is estimated to be in focus and therefore the corresponding depth is assigned. In [99] we take advantage of the possibility to generate a focal stack from the plenoptic frame captured after a single shot, as

shown in Fig. 4.2. An additional advantage of FiMic is its characteristic of providing directly EIs that have all the scene in focus. This gives an advantage over conventional implementations of DFF concept, since now it is not necessary to use sharpness measurements, but we can compare each slice of the stack with the all-in-focus image. Therefore, an area-based comparison with a window of $n \times n$ pixels is used to reduce ambiguities [102], due to noise inherent to the capture process. The intensity pattern of the window applied to the $(x', y')_{EI}$ of central EI is compared with the correspective $(x', y')_{FocStack}$ of the computed images of the focal stack. The metrics used to compare the two windows is the normalized cross-correlation (NCC), because it is more robust in terms of noise than cross-correlation and photometric differences than distance-based measures [103], such as the sum of absolute differences (SAD) and the sum of squared differences (SSD). The maximum value outputted by the NCC is obtained when a best match is recognised and therefore the window of the focal stack is in focus. Following this rule the depth is assigned to the (x', y') central pixel of the window. If more than one maximum is obtained for a given pixel, a selection criteria of neighbors consistency has been adopted. Doing this process to all the pixels a dense depth map is generated. All the details of the mathematical derivation can be found in [99].

4.2.1 Occlusion handling algorithm

It must be reminded that with lightfield microscopy the sample is imaged from different perspectives, implying that some parts of the object, that are hidden in the central EI, might appear in other EIs or vice versa. This suggests us not to calculate only a single depthmap, but to take full advantage of the information captured iterating the process. Concerning the algorithm, it means that the depth-map generation, can be repeated but changing the central image chosen for the focal stack generation and comparison. This process is looped for all the EIs, providing an equivalent number of complementary depth-maps as shown in Fig. 4.3. Therefore, to reduce the impact
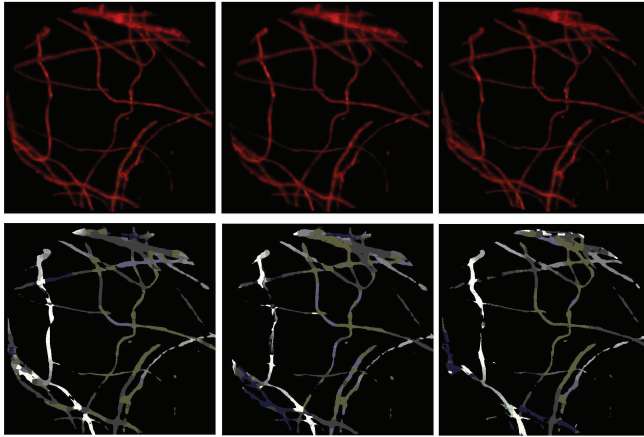
Figure 4.3: Examples of depth maps (below) generated for the different EIs (above)

of the error in the depth-map, we collect information from all the perspectives and merge them together into a virtual space. This has a double effect, it makes the algorithm more robust, but also allows to handle possible occlusions since the information is gathered from many different perspectives. After calculating all the depth-maps, the generation of the virtual space is done by back-projecting, through the system parameters, all the pixels of the depth-maps into a virtual space called point-cloud:

$$d(x', y') = d(x, y) \tag{4.3}$$

where $d(x', y')$ and $d(x, y)$ are respectively the depth of the point-cloud P at (x', y') and depth-map at (x, y). The correspondence among the two coordinate spaces is held by the following equation:

$$(x', y') = (x + m'_x \times s_x, y + m'_y \times s_y) \tag{4.4}$$

where $\mathbf{m} = (m_x, m_y)$ is the vector that accounts for the index of a given microlens and $\mathbf{s} = (s_x, s_y)$ is the vector that accounts, depending on the assigned depth, for the shift in the x-y directions. In cases
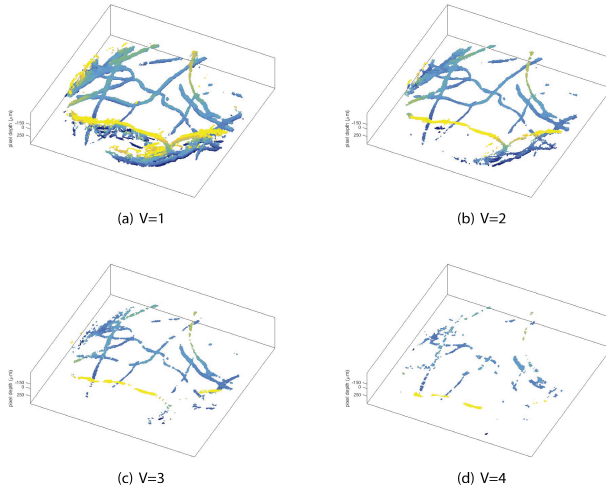
(a) V=1

(b) V=2

(c) V=3

(d) V=4

Figure 4.4: 3D Point-clouds generated by merging all depth maps with different voting thresholds V

with an occlusion, the object is detected only by a portion of all the EIs, and only unoccluded pixels can converge to a single point with the same intensity. Whilst, occluded pixels, when back-projected, will reach a point in the point-cloud that does not have photometric consistency with the original image. Taking into account these properties, an easy way to improve the robustness of the algorithm is to introduce a voting scheme, if a point in the point-cloud is reached, at least, by the projection of a number V of depth-maps, then it is stored in the point-cloud P, otherwise is omitted. If V = 1 no voting scheme is performed, if $V = \#EIs$ (number of EIs) then the density of the point-cloud is likely to be reduced a lot, since errors in the computation of the depth-maps are still present. Therefore the ideal V is a number in between those two extremes.

4.2.2 Experimental verification

To test our proposed method a FiMic was built with an hexagonal-shaped MLA, and seven EIs fitting into the AS. The ORP is indicated as $d_f = 0$, and a full pixel disparity corresponds, following Eq.(4.1), to a $\Delta z = 14.5\mu m$ in depth. Fluorescent cotton fibers have been used as sample object and the focal stack has been calculated for 25 different depth planes within the DOF of the system. Fig. 4.2 shows some slices of the stack where different fibers come into focus. In Fig. 4.3 we show the depth-map extracted using three different EIs as central image for the computation of the focal stack. Finally in Fig. 4.4 it is possible to see the different point-clouds obtained changing the value V of the voting scheme. Clearly increasing V implies a reduction in the density of the point-cloud.

4.3 Optical-sectioning microscopy through single-shot lightfield protocol

Aiming to allow certain competition with confocal microscopy, next, we propose a novel algorithm with the capability of providing depth images with optical sectioning. However, being aware of the enormous difficulty of facing this challenge without the use of scanning procedures, we moderate our ambition and restrict the applicability of our protocol to the case of sparse fluorescent samples over a black background. Another feature of our proposal is the computation speed, which allows to produce and to show, in real time, depth images with optical sectioning. All of this is possible through a smart, minor, change in the S&S algorithm. The functioning of the new algorithm is the same as the S&S but substituting the sum step by a multiplication (and adequate normalization), of the pixels. All the theoretical explanation is formally derived in the published Article [IV]. Here we focus our effort in explaining what is the reason for this minor change, and why it is so effective. To understand this, we can start by observing that, when the sample is sparse and fluorescent, it
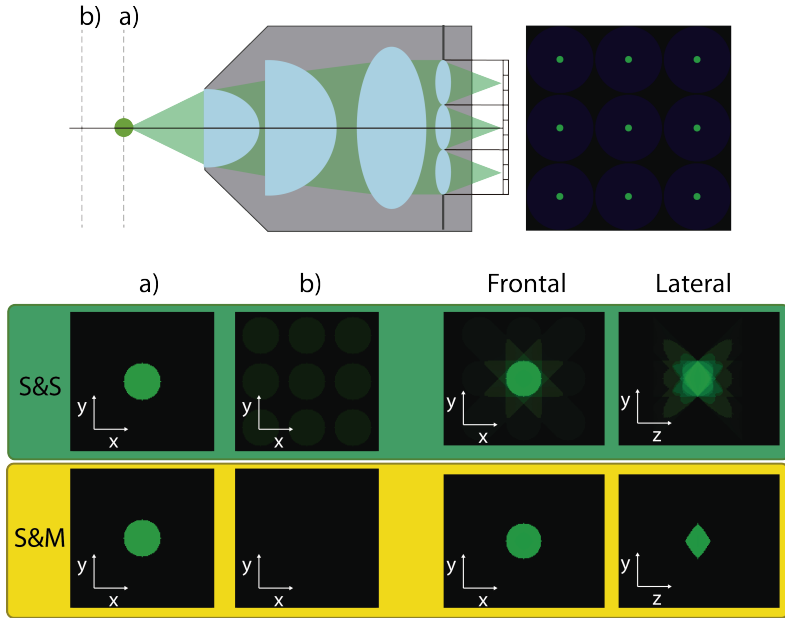
Figure 4.5: On the top part of the image is shown a compact FiMic schematic with a green circle in the optical axis; two planes a) and b) at different depths; and the simulated capture of 9 EIs. On the bottom are shown the outputs of the two algorithms S&S and S&M at the selected depth planes a) and b). Moreover the volume computed (through MIP) is shown in its frontal and lateral view, showing how S&M eliminates the noisy background.

can be thought as a simplified scenario where there is only one object present, and nothing else close to it, emitting light and a black background around it. To describe this situation we can use the simulated scenario of Fig. 4.1, and simplify it considering only one fluorescent circle as in Fig. 4.5, note that it is not relevant its the depth position as long as it lays within the DOF. Applying the S&S and S&M algorithms to the plane where all the circles coincide with no disparity in the EIs (e.g. depth plane a) in Fig. 4.5) will certainly output the same information as in Fig. 4.5 a). What makes the difference in the two algorithms is the result in out-of-focus planes (e.g. depth plane
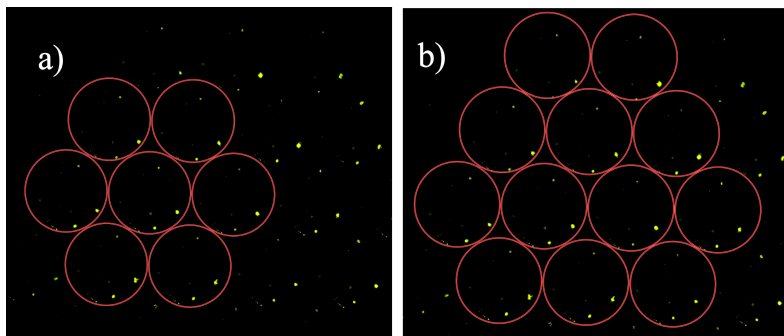
Figure 4.6: Elemental images captured by the sensors. In a) and b) the algorithm respectively selected 7 and 12 EIs.

b) in Fig. 4.5). In the case of plane b) it is possible to understand the different outputs that the two algorithms deliver. When applying the S&S, the images will be shifted towards the central one and their intensities summed and normalised. Then, when the shifting does not exactly coincide with the one corresponding to the depth plane of the object, replicas of the object appear, in this example nine circles whose intensity, due to normalisation, is $1/9^{th}$ of the original one. On the contrary, when the S&M algorithm is applied to the same depth plane b), the intensities are not summed but multiplied, which means that there is going to be at least one multiplication by zero (black background). The result is a black depth-reconstructed image, as desired. These facts are even more evident when the full focal stack is computed and 3D volume is rendered through a MIP algorithm, as shown in Fig. 4.5 in the *Frontal* and *Lateral* views of the 3D reconstruction.

4.3.1 Experimental verification

In order to prove the S&M algorithm, two experiments were implemented: one with beads and another with cotton fibers. In both experiments the sample was stained with a fluorescent dye. For a
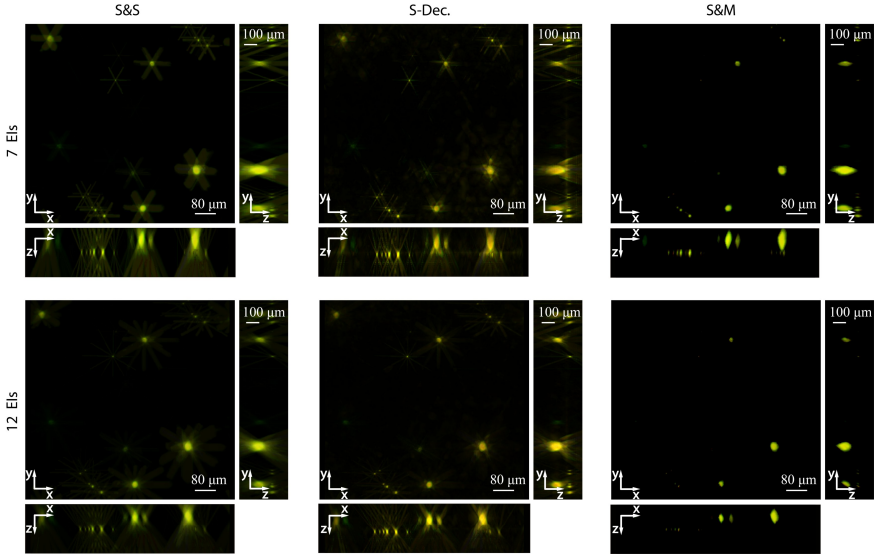
Figure 4.7: Front and lateral views of the simulated 3D render obtained from a z-stack calculated using the S&S backpropagation method (left) the S-Dec (central) and the S&M (right) for 7 and 12 EIs, respectively on top and bottom row.

complete analysis, the proposed S&M was compared with the standard S&S and with an algorithm proposed by our group of research based on 3D-deconvolution (S-Dec) [104]. The two setups for the experimental validation are detailed in the Article [IV], here we report the results in order to be able to describe and analyse them. For the first experiment we prepared a sample in which some fluorescent beads were randomly distributed. Then using the FiMic setup, equipped with an hexagonal MLA, we captured a lightfield image composed by several EIs. Then we aimed to prove the efficiency of the algorithm and also to analyze the influence of the number of EIs utilised. The lightfield capture can be seen in Fig. 4.6. Two cases a) and b) mimic a capture with seven and twelve EIs respectively. What is expected from the output of the algorithms is that the second case
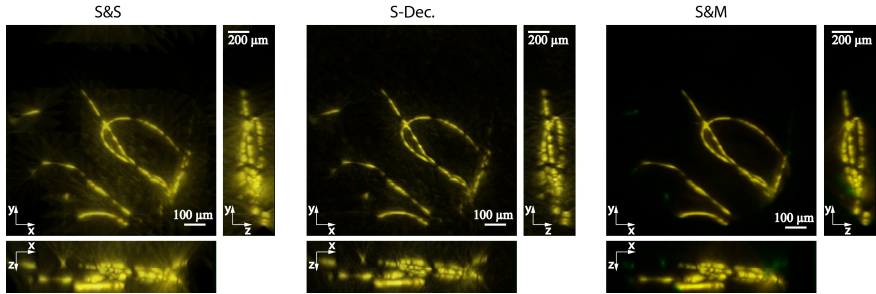
Figure 4.8: Comparison of different methods applied to cotton fibers recon-struction.

will have a better depth resolution of the objects as Eq.(9) of Article [IV] suggests. The results are shown in Fig. 4.7, and three things can be confirmed from these images:

1. S&M shows better optical sectioning compared with the other two algorithms

2. As the number of EIs increases the optical sectioning improves

3. The depth resolution is also dependant on the size of the object

The same conclusions are evident from the second experiment, where cotton fibers were used as sample, Fig. 4.8. Finally, in order to give a quantitative parameter that confirms the results, visually perceivable from the figures, we plotted the axial curve response for the beads and the fibers (Fig. 4.9), confirming that S&M performs a much better optical sectioning, as result of the efficient removal of the background noise proceeding from the out-of-focus planes.

4.3.2 GPU speed improvements

The goal of this system, comprehensive of the FiMic with the S&M, is to give the user of the microscope a tool that can provide real-time results during the analysis of the sample. In order to achieve our
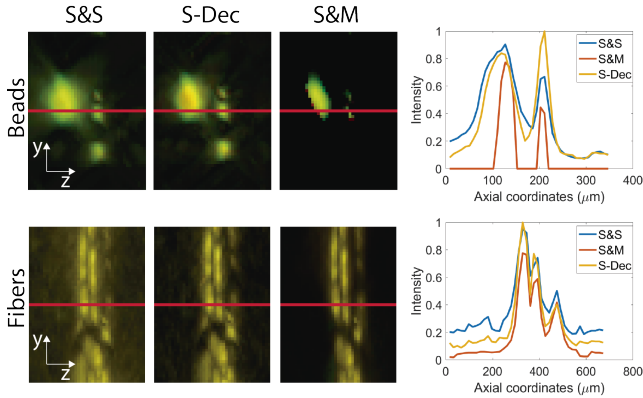
Figure 4.9: Axial curve response for the three different algorithms, for the experiment with the beads (top row) and the fibers (bottom row). The plots represent the intensity of the images along the red line.

goal we adopted GPU-parallel computing, a technique broadly used in computer graphic, that allows to drastically boost the computation time of the algorithm. What makes GPUs very interesting is their highly parallel structure that is optimal for algorithms that can be split in smaller and independent blocks to be processed in parallel. For the mentioned reasons, in the development of this Thesis, GPU computing was introduced with the aim of optimising the speed of the optical sectioning protocol. The goal of this implementation is to give the user of the microscope the possibility of arbitrarily selecting (in real-time) the depth of the sample to be displayed. As mentioned earlier, the algorithm consists in shifting the EIs towards a central one, multiplying the intensities of the superimposed pixels and properly normalising the result. It is easy to deduce that, since each pixel of the calculated depth-section is independent with respect to its neighbors, parallel processing is applicable. A special care must be given to the specifications of the system, since it will influence its optical performances from one side and its computational performances on the other. As a matter of facts we have already discussed that in-
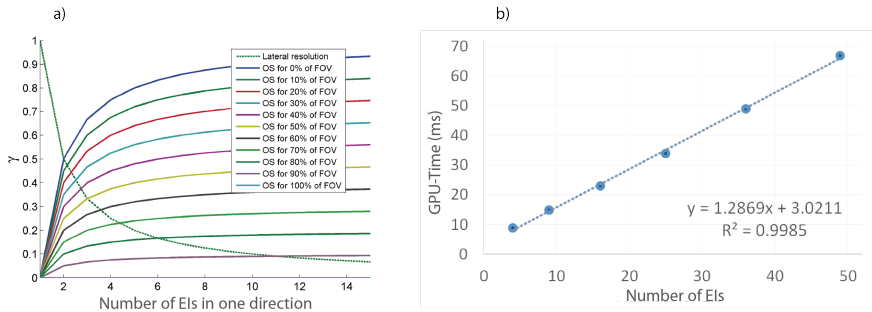
Figure 4.10: a) Curves of the γ value for the lateral resolution and optical sectioning as a function of the number of EIs and the field-of-view occupied by the sample. b) The speed of the algorithm is linearly dependent on the number of EIs used in the reconstruction, and is shown with experimental data fitted with a linear curve.

creasing N (number of microlenses in the diagonal of the AS) reduces the lateral resolution and increases the DOF, this, of course has an impact also in the computation algorithm, since each pixel requires a number N×N of multiplications it will influence the speed of the output. In order to evaluate both factors, two graphs have been drawn as a function of different number of EIs: the first one (Fig. 4.10(a)) shows the optical performances; the second one (Fig. 4.10(b)) the computational time. In the first graph, by means of Eq.(9) of Article [IV], we plotted the lateral resolution and the optical sectioning (OS) as a function of N. The parameter γ evaluates, in relative terms, the lateral resolution or the optical sectioning. As known, the lateral resolution of EIs decreases proportionally to $1/N$, as shown through the decreasing dotted green curve. The optical sectioning is evaluated by calculating the axial extent of the reconstruction of a plane sample object. Naturally this extent is minimum when the object is a single point (0% of the total FOV) and the number of EIs tends to infinity. Thus, this is the normalized extent that helps to define γ when evaluating the optical sectioning. To account for the size of the object, curves are plotted corresponding to different percentage of the FOV

occupied by the object. The curves show that for point objects the optimal tradeoff for resolution and optical sectioning occurs for the case of point objects and 2×2 EIs, and it make sense since it implies minimum resolution reduction and capability of optical sectioning. In other cases of sparse sample it can be assumed that the object will not exceed 10% of the FOV and therefore the optimal case would be around 3×3 EIs, and as already mentioned, the bigger the size of the object, the less optical sectioning achievable. The second graph instead shows the behaviour of the algorithm in terms of speed with respect to the total number of EIs utilised. We evaluated the computation time increasing the EIs implied. The result shows a linear dependence. We can conclude that depending on the needs of the user and the specifications of the sample the number of EIs might vary as follows:

- For better lateral resolution and speed the number of EIs must be low at the cost of optical sectioning performances

- For better optical sectioning the number of EIs must be high at the cost of lateral resolution and speed

One last comment might be done regarding the S&S algorithm, which would provide the same timing results as the S&M but with much lower optical sectioning quality.

4.4   What about super-resolution in FiMic?

There are some situations in microscopy that require big sensor pixels, because in general there is a relation of proportionality between the pixels' area and their signal to noise ratio (SNR). Then, for those cases of low light-emission rate it is very important to increase the SNR. In conventional microscopy this is not a problem, because the image projected onto the sensor is strongly magnified, so that the pixel size is much smaller than the Airy disk at the image plane. This is not the case in FiMic, where the focal lengths of the MO

and the microlenses are of the same order of magnitude. In such case the big pixels of the sensor do limit the resolution capability more than the diffraction limit. Take into account, besides, that in FiMic a number N of lenslets are introduced in the diameter of the AS, so that the effective NA is reduced by the same factor. This reduces by factor N^2 the amount of light reaching the sensor from any emitting point. The good news is that when the size of the pixel is greater than the diffraction spot, the undersampling of the sensor, causes sub-pixel shifts of the objects between the EIs, and this aliasing patterns can be used in computer vision in order to retrieve sub-pixel resolution in the final result [83]. In this sense we analyze the sampling patterns of FiMic with the scope of introducing computational super-resolution with deconvolution trying to improve the results obtained with classical reconstruction algorithms. In literature there are several contributions made in computational super-resolution obtained with aliased low resolution images captured with sub-pixel camera shifts [105–107], or with sub-lenslet shifts in classical lightfield microscopy (iMic) [83, 93, 108, 109]. From Eq.(3.11), which defines the limits of resolution due to the pixel size, we can introduce a super-sampling factor $s \in \mathbb{N}$ that influences the sampling rate of the reconstructed volumes, meaning that the resulting voxel pitch will be:

$$\delta_{super} = \frac{\delta_{pix}}{s} \qquad (4.5)$$

In order to make the reconstruction, it is important to capture enough EIs with different aliasing patterns, providing sufficient sampling [110–112] of the aliased object. In the Article [V] we described in detail the wave-based forward light propagation model that evaluates the PSF of the system, from a point source, through the FiMic parameters, till the imaging sensor. Important considerations that help reducing the complexity of the systems must be made: (a) we assume that the PSF is smaller than the pixel size and therefore the effect of aberrations is considered negligible; (b) positioning the MLA at the AS of the systems makes any EI of the FiMic linear and translation-

ally invariant, and considering all the lenslets identical, this makes the whole FiMic system characterized by a single PSF. Once the PSF is modeled, it can be fed to the deconvolution algorithm which will restore the better-resolved image. The algorithm is based on the well known Richardson-Lucy algorithm [113, 114] and estimates de discretized volume **v** of the sample with an iterative procedure Eq. (12) in Article [V]:

$$\mathbf{v}^{q+1} = \frac{\mathbf{v}^q}{A^T \mathbf{1}} \left[A^T \frac{\mathbf{m}}{A \mathbf{v}^q} \right] \qquad (4.6)$$

where the operator A describes the lightfield forward model, **m** represents the lightfield measured at the sensor and q is the iteration count.

4.4.1   Experimental verification

To validate our algorithms two experiments have been designed; the first one with a resolution target (USAF-1951) displaced in depth, and the second one using cotton fibers stained with a fluorescent dye.

a) USAF-1951

This experiment was performed with a FiMic composed of: an infinity corrected MO with $f = 9.0 \ mm \ (20\times)$ and NA = 0.4; a relay system with $f_{RL1} = 125 \ mm$ and $f_{RL2} = 200 \ mm$; an hexagonal MLA with $f_{ML} = 6.5 \ mm$ and $p = 1.0 \ mm$ (APH-Q-P1000-R2.95 manufactured by AMUS); and a CMOS camera (EO-5012c 1/2") with 2560x1920 square pixels of $\delta = 2.2\mu m$ in side. With this configuration we obtain $N = 11.5, \rho_{geom} = 9.7 \ \mu m$ and this should permit to resolve the target groups 6.5 and 7.2, respectively. We captured a collection of images at different depths from the $\Delta z = -120\mu m$ till $\Delta z = +120\mu m$ with a $10\mu m$ step. In Fig. 4.11(a) we display at different depths $\Delta z = \{0, -20, -50, -100\}\mu m$ the central EI, and the results obtained with the S&S algorithm and with the proposed deconvolution algorithm applying two super-sampling coefficients s=1 and s= 3. We see that in case of S&S the resolution is limited to group 6.4, which corresponds
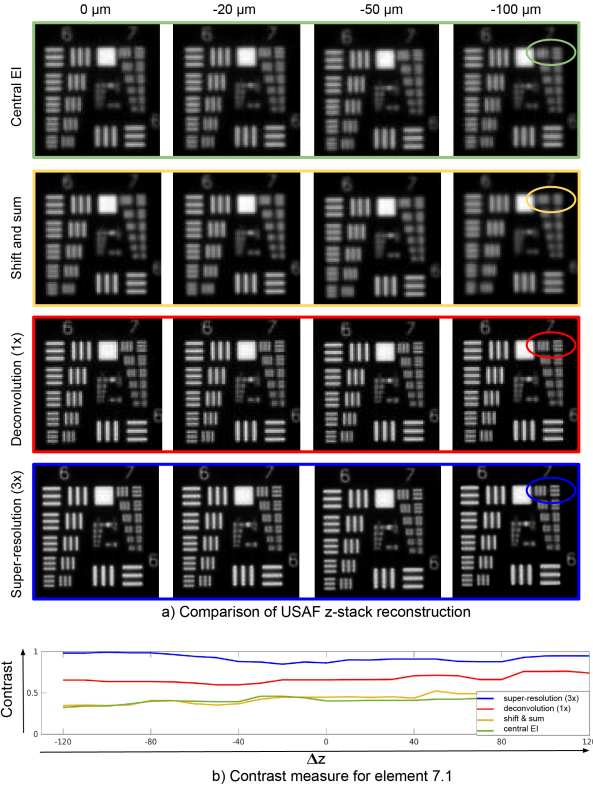
Figure 4.11: *Reconstruction of the USAF 1951 target imaged at* $\Delta z =$ $[-120, 120]\mu m$. *a) Central EI of the FiMic image (green), the refocused image (yellow), the deconvolved image at sensor resolution (red), and at 3× sensor resolution (blue) for axial positions* $\Delta z = \{0, -20, -50, -100\}\mu m$. *Element 7.1 appears resolved in the super-resolved image (blue oval). b) Contrast of the USAF element 7.1 over* $\Delta z = [-120, 120]\mu m$ *is generally constant for all the methods in a). As expected, the super-resolved deconvolution shows the best contrast.*

to $11\mu m$, whilst for the deconvolution with s=1 and s=3we reach group 6.6 ($8.8\mu m$) and 7.1 ($7.8\mu m$) respectively. Additionally, in order to characterize the behaviour of the algorithms through all the

a) Raw image

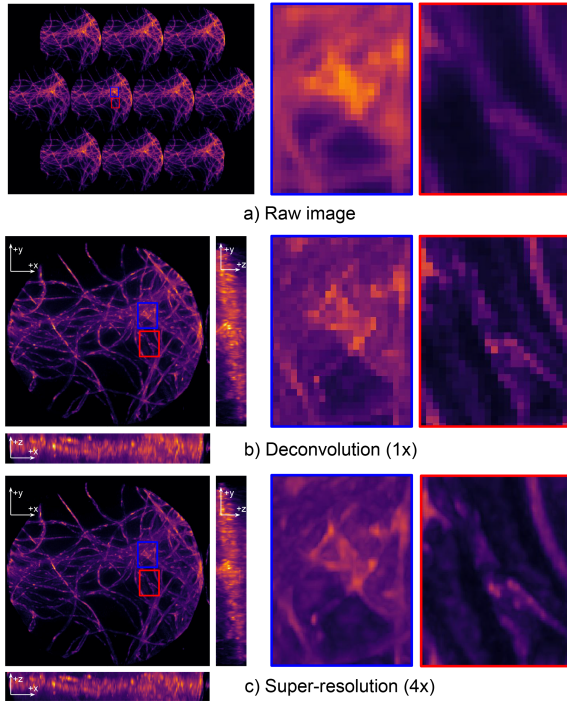b) Deconvolution (1x)

c) Super-resolution (4x)

Figure 4.12: 3D reconstruction of cotton fibers. a) Raw image acquired with our experimental FiMic setup and zoomed-in regions of an EI for details. b) Maximum intensity projections (MIPs) and zoomed-in regions of the 3D reconstructed sample ($\Delta z = [-150, 150]\mu m$) using our proposed method at sensor resolution ($s = 1$). c) MIPs of the super-resolved 3D reconstruction at $4\times$ sensor resolution ($s = 4$). The deconvolved images resolve structures structures that do not show in the EI. The close-ups in b) and c) clearly shows that the super-resolved reconstruction recovers fine details in the sample, that are not resolved in the normal deconvolution.

depth acquisitions in Fig. 4.11(b) we plotted the computed contrast measured for the element 7.1. This measure shows that FiMic is stable throughout a great depth range, but also confirms the optimal results obtained with our reconstruction method.

b) Fluorescent cotton fibers

The design of the FiMic for this experiment is the same as the previous one, with the exception of the relay, that now is composed by lenses with $f_{RL1} = 50\ mm$ and $f_{RL2} = 40\ mm$. This results in a $\rho_{geom} = 4.9\mu m$ and $\rho_{diff} = 4.9\mu m$ considering $\lambda = 680nm$ for red light. Since for this experiment the requirement of having the resolution limited by the pixel was not met, we made a post-processing binning (2×2) of the image, resulting in a doubled pixel size and $\rho_{geom} = 9.8\mu m$, well above the diffraction limit. In Fig. 4.12(a) we show the lightfield capture as well as two zoomed-in regions. The sample was reconstructed from $\Delta z = -150\mu m$ till $\Delta z = +150\mu m$ with $10\mu m$ steps at super-sampling rates s=1 and s= 4 in Fig. 4.12(b) and (c). In both cases we see an improved resolution, but clearly the scenario with s=4 gets the overall best results. Of course in those experimental setups where diffraction and pixel resolution are comparable, the sub-pixel aliasing patterns are negligible and therefore computational super-resolution has a minor impact.

4.5 Robust depth estimation for lightfield microscopy

Until now,x the described algorithms were developed for the specific case of fluorescent sparse samples, a situation that is very common in microscopy but that does not cover all the possible cases. For this reason a more robust algorithm has been thought in order to be more flexible to different type of samples, aiming to cover a more vast scenario of possibilities. Detailed information of all the steps of the algorithm are described in the published article Article [III]. Here the different steps and blocks will be described in order to give an understanding on the choices made to develop the algorithm. As previously mentioned, many algorithms have already been developed for the macroscopic scale and behave very well for those scenes that are colorful and rich of texture, but exhibit a lot of noise if directly ap-
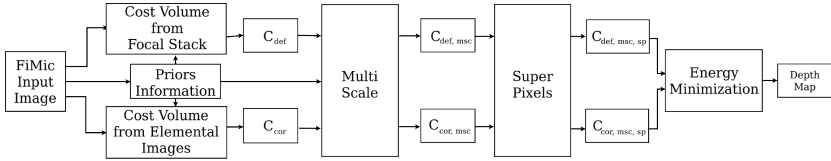
Figure 4.13: Pipeline of the depth estimation process. The name of cost volume (e.g., C_{def}, C_{cor}) are consistent with the ones used in the paper.

plied to microscopic samples. Therefore, the idea is to take advantage of the knowledge built upon those techniques, and apply them to microscopic samples but with some additional steps and corrections that make the estimation more robust. The framework can be divided in three main steps. The first one is the generation of two cost volumes using two different focal cues: defocus and parallax correspondences. The second one is the application of filtering methods that use multi-scale approach and super-pixels cost aggregation in order to enhance robustness and reduce computational noise. The last one consists in merging the two filtered depth-maps through a multi-label optimization. Fig. 4.13 shows in detail the pipeline of the framework. Given a lightfield image from FiMic two cost volumes are built, one using the depth cue of the defocused objects of the focal stack and the second one using matching criterias along epipolar-planes of the images. Some prior information is given to the algorithm in order to better adapt the results for the different cases of sparse or dense samples. For example a matting mask, composed of ones where the object is present and zeros where there is an empty space, avoids to make calculations in the dark regions void of real information. Besides, areas with high or low frequencies are discriminated in order to calculate high or low-resolution depth estimation. The two cost volumes are then improved using a multi-scale approach, allowing to shape the cost volume in function of some characteristics of the pixels, e.g., if a pixel belongs to a high or low frequency area its cost will be characterised respectively from the higher or lower resolution grouping schemes. Additionally, in this step, pixels with similar character-
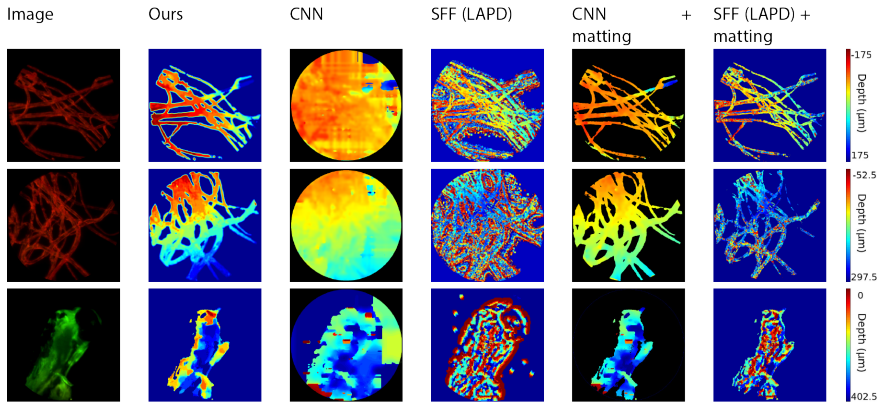
Figure 4.14: Comparison with Neural Networks (CNN) [115] and Shape from Focus (SFF) [116] on dataset of biological samples: first two rows consist of cotton fibers, last row is the head of a zebrafish.

istics are grouped in superpixels which can be treated in two ways. Choosing a small size for the superpixel one can define it belonging to one plane, while selecting a bigger size allows to assign more than one plane (assumably close planes for continuous objects) within the same superpixel. Once the two cost volumes are computed and optimally filtered, they are merged through an energy minimization approach. An energy function that combines both cost volumes is built and a minimum value is searched through a multi-label optimization approach. Finally, a post-processing filter that uses a median filter and a guided filter can be used to obtain a smoother depth map if needed.

4.5.1   Experimental verification

To validate the proposed framework we compared with state-of-the-art algorithms for stereo matching and depth from defocus. We first compared for the case of fluorescent sparse samples in Fig. 4.14, and secondly for the case of dense samples in Fig. 4.15. The first set of images (Fig. 4.14) deals with three fluorescent biological samples: two are cotton fibers stained with fluorescent dye and a the third is the
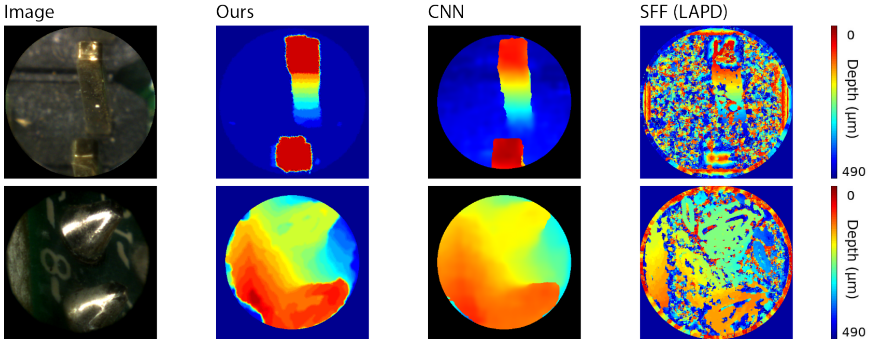
Figure 4.15: Comparison with CNN [115] and SFF [116] on dataset of opaque electrical components.

head of a zebrafish. In all the cases the targets are stimulated with a monochromatic light beam proceeding from a laser and are emitting light with longer wavelength. A bandstop filter blocks the illumination beam in the capturing stage and let the light emitted from the sample to reach the sensor. The results demonstrate that direct application of depth estimation algorithms for macroscopic images fails to succeed for thin samples with black background and repetitive patterns (like with the fibers). To ensure a fair comparison, we added our matting procedure to the estimated depth maps, showing more consistent results. This improvement confirms the quality and robustness of our approach in estimating the depth if extra precautions (the mattinng mask in this case) are applied also to other algorithms. Since this algorithm was designed to be flexible for different sets of images, we decided to capture the lightfield corresponding to small opaque electrical components (Fig. 4.15), which in this case will lack the dark background and thin repetitive structures. From the results of these images we can make some considerations: depth map calculation is highly challenging and simple approaches like shape from focus [116] outputs very noisy results, while more complex approaches that incorporates filtering steps as [115] reach better results with comparable outputs.

Figure 4.16: Synthetic images generated with Blender. They simulate the behaviour of the FiMic, for the case of fluorescent fibers

4.5.2 Computational verification

Even though these results show a good behaviour, we still need the comparison with some sort of ground-truth image. To allow this, it was necessary to generate computationally a 3D volume and its relative lightfield capture. We have chosen to use Blender [117], a program widely used to simulate lightfields, in order to obtain a realistic capture of the fibers. Fig. 4.16 shows different simulated scenarios. The results, compared to the ground truth, are presented in Table 4.1. The estimation as well as its standard deviation are lower

Approach	Error	Standard Deviation
Ours	2.32555	1.8154478
CNN [115]	2.4275436	2.4392762
SFF [116]	9.379839	4.1694072

Table 4.1: Table with resuts from synthetic images

for the proposed method, confirming the improvement in accuracy and robustness. The neural network algorithm (CNN) [115] reaches similar performances in terms of the error but with greater variations, as demonstrated by the standard deviation. The shape from focus (SFF), as can be expected, presents the worst behaviour as it lacks any post-processing steps.

Chapter 5

Application of the FiMic

In this section we introduce an interesting application of FiMic we have developed during this Thesis. Since our goal is to provide a 3D microscope that can be as versatile as possible, we wanted to expand the number of samples that this system could analyse. Until now we have presented results captured mainly through two illumination configurations: brightfield and fluorescence. Our intent now is to investigate the possibility of getting informations from semi-transparent and phase objects. To deal with this scenario we have adapted the FiMic architecture to dark-field illumination concept.

5.1 Dark-Field FiMic

It is usual in microscopy to deal with specimen that has, under normal illumination, very low contrast. In other words, it is highly transparent and therefore no distinguishable image can be obtained. To enhance the contrast or to discriminate parts of the sample, different techniques can be applied. One easy and common approach is to stain the sample with a fluorescent dye and capture the light emitted by the fluorophores. But staining is not always possible or recommendable. In this case, a common way to distinguish transparent objects is to use dark-field illumination [118]. In a very sim-
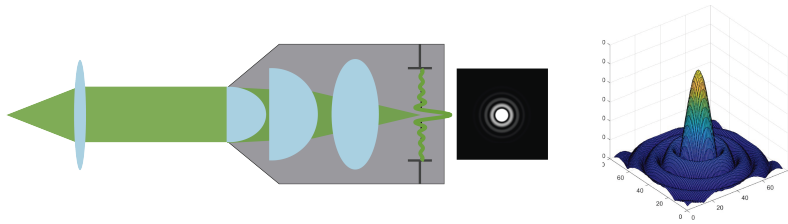
Figure 5.1: Example of conventional illumination, where a monochromatic point source is projected onto the AS, due to the finite size of the optical elements the image of the point will result in an Airy disk.

ple scheme, dark-field imaging is based on blocking part of the light beam emitted (or diffracted) by the sample in such a way that the zero-frequency component of the object spectral information does not reach the sensor. The resulting image is the high-frequency content of the sample, and shows its edges and structures. Our aim here is to apply the dark-field concept to lightfield microscopy imaging. More specifically, we consider that FiMic architecture is specially suited for dark-field implementation. Take into account that the MLA is placed at the Fourier plane, and therefore it will be easy to operate over the spectral information of the sample and, more specifically, to block the zero frequency component. Let us consider the ideal case in which a converging lens receives the light proceeding from a monochromatic point source, as shown in Fig. 5.1, and produces a collimated beam that illuminates, under normal incidence, the MO. Due to the finite size of the lenses, at the Fourier plane of the MO (which for an infinity-corrected MO falls at the AS) appears the diffraction image of the point source; an Airy disk. If we now place a transparent object at the front-focal plane of the MO, what we find at the AS is the convolution between the object spatial spectrum and the Airy disk. A way of blocking the zero-order spectral component, is to insert an opaque mask at the center of the AS. This way of proceeding implies, however, to perform physical modifications over the MO. An alternative procedure relies in the modification of the illumination beam,
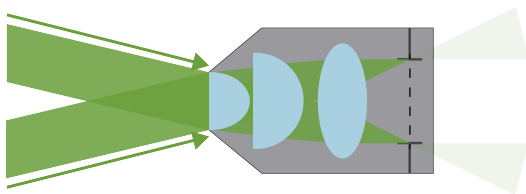
Figure 5.2: Example of illumination beam obtained with a ring, whose image lays just out of the AS, in order to provide correct cancelation of the zero-order spectral components

so that the zero-order component is blocked by the opaque area of the AS. This can be made by using, not a point source, but a ring source with a diameter such that its image falls just out the AS, see Fig. 5.2. We can consider that the ring is composed by infinite number of point sources. Therefore, infinite replicas of the spectrum will now be present at the AS plane, but in all of them the zero order is physically blocked by the AS itself. Then, placing the tube lens at its position, the fourier transform of this superposition of high-frequency content is formed at the sensor. Thus, at the sensor we have the image of the sample, but free from the zero-order spectral component. This permits, among other effects, the visualization of phase variations of transparent specimen. The implementation of dark field in FiMic is very easy. Since in FiMic any microlens behaves as the tube lens, we only need to illuminate the sample with the illumination ring and capture the lightfield image. Proceeding in this way a collection of EIs, all free from the zero-order spectral component, is captured. Then all the algorithms described above can be applied, but now for obtaining the 3D map of transparent samples.

5.1.1 Experimental validation

For the experimental validation, we used the same FiMic setup as in Section 4.3 but changing the illumination mode. As transparent sample we used soap detergent that had been shacked in order to obtain bubbles of different sizes and at different depths. In Fig. 5.3
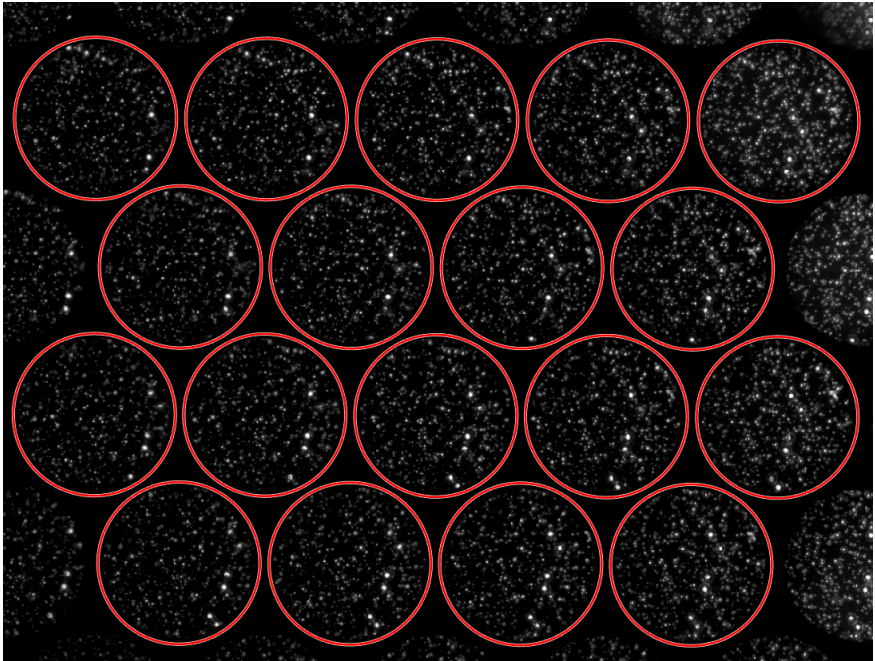
Figure 5.3: Lightfield image of a soap detergent that had been shacked in order to obtain bubbles of different sizes and at different depths.

we show the captured lightfield image. Thanks to the illumination ring, the dark-field capture allows to get an high-contrast image of bubbles that would have very low contrast otherwise. It is possible, then, to see the usefulness of implementing DF-FiMic, when the 3D reconstruction of the sample is performed. A powerful tool is given by the shift and multiply algorithm known as S&M [119], which in this cases is able to provide optical sectioning of transparent samples in real-time. As shown in Fig. 5.4, a 3D volume is reconstructed and it is possible to see the sample rotated by any arbitrary angle, in this case 0, 45 and 90 degrees are shown. Finally in Fig. 5.5, captions at different depth section of the bubbles are shown.

Figure 5.4: 3D volume is reconstructed and it is possible to see the sample rotated by any arbitrary angle, in this case 0, 45 and 90 degrees.

Figure 5.5: Captions at different depth section of the bubbles.

Chapter 6

Conclusions

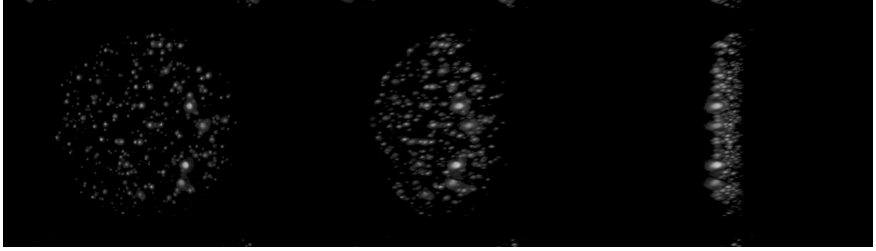Nowadays, there are many scientific research fields dedicated to the acquisition of the spatial and depth information of 3D scenes. One of those techniques that is promising a big development for the near future is lightfield imaging, firstly thought for big scenes of the real world and subsequently adapted successfully to the capture of microscopic 3D samples. In the development of this Thesis, we dedicated our best efforts to contribute to the growth of the knowledge in lightfield microscopy, by combining work dedicated to the optical system as well as to the development of new algorithms. The proposals of this Thesis are an original and genuine contribution to this research field, as demonstrated by the publication in different articles in high-impact journals. To begin with, we started with the study of the classical implementation of the iMic. Underlying its promising capability and at the same time its technical limitations. To give the reader a deeper insight to the analysis built during the Thesis, we started with an introduction of the conventional microscope, underlying its properties in terms of two fundamental parameters: lateral resolution and depth of field. Once these parameters have been defined, and once the principles of iMic were introduced, it has been made clear that the gain of 3D reconstruction came at some cost, specifically in the achievable lateral resolution. Those limitations, unfortunately are inherent

to the optical system and cannot be resolved in a simple manner, resulting in reduced performances in terms of lateral resolution and depth of field of the acquired images. Those limitation, triggered the interest of a vast community of researchers whose intent have been to overcome them with some smart algorithms capable of increasing the resolution and depth of field computationally. An experiment built in our laboratory showed that the use of a tunable liquid lens, allows to increase the depth of field, making this technology more interesting from the volumetric reconstruction side, but less appetitive since we are trading capturing speed for the increase in captured volume. Therefore we decided to go a step backward and rethink the optical system of the lightfield microscope, and we came up with the new FiMic design, based on the shift of the MLA position, from the image space of the microscope, to the Fourier plane of the microscope objective. Thanks to this new implementation, we demonstrated that an optical solution to those drawbacks is desirable in order to have a capture that is already outperforming the best outputs of the old configuration (iMic + dedicated algorithms). On top of that, additional algorithms may also be applied to the new design obtaining a further overall improvement. In our very first implementation of the new optical solution we built a very raw prototype of the FiMic, where, to demonstrate the applicability of the proposed principles a time multiplexing with a moving camera was done. Given the very promising results, we decided to make a step forward in the design, implementing the system with an MLA. This implementation did not came without efforts, since it was a completely new system and many parameters needed to be defined and undertanded. Once the performances of the new system where clear, we decided to make an experimental comparison between iMic and FiMic, which confirmed what we supposed through theoretical derivations, meaning that performances in terms of lateral resolution and depth of field, resulted to be improved. On top of that, the FiMic system is more user friendly, since it was very easy to adapt it to different needs, depending on the sample under inspection. In the meanwhile, we did not focus our

work only in the implementation setup, but also in the algorithms for the final 3D reconstruction. There is a big community working on lightfield reconstruction in the macroscopic scale, but those contributions are not easy to apply directly to microscopic samples, due to the different characteristics of the image acquired. For this reasons ad-hoc algorithms have been proposed to optimally threat a variety of samples that can span from fluorescent sparse samples (monochrome sparse image) till opaque reflecting objects (components of an electronic chip). Due to the different nature of the mentioned scenarios, different algorithms have been proposed to tackle the specific problems, this is not an issue since a microscopist whose intent is usually some fluorescent sample, will not easily need to change suddenly and analyze a completely different kind of sample.

To conclude we believe that the next research efforts must be made to find useful implementation for specific cases, meaning to customize even further the optical design and especially the reconstruction algorithm for particular samples commonly used in different laboratories. To achieve this goal, we believe that a growing tool to include in the system are artificial intelligence algorithms, capable of excellent performances in a short computational time.

Bibliography

[1] C. Wheatstone, "Contributions to the physiology of vision.," in *Abstracts of the Papers Printed in the Philosophical Transactions of the Royal Society of London*, vol. 4, pp. 76–77, JSTOR, 1837.

[2] W. Rollmann, "Notiz zur stereoskopie," *Annalen der Physik*, vol. 165, no. 6, pp. 350–351, 1853.

[3] S. S. Kim, B. H. You, H. Choi, B. H. Berkeley, D. G. Kim, and N. D. Kim, "Invited paper: World's first 240hz tft-lcd technology for full-hd lcd-tv and its application to 3d display," in *SID Symposium Digest of Technical Papers*, vol. 40, pp. 424–427, Wiley Online Library, 2009.

[4] H. Kang, S. Roh, I. Baik, H. Jung, W. Jeong, J. Shin, and I. Chung, "3.1: A novel polarizer glassestype 3d displays with a patterned retarder," *SID Symposium Digest of Technical Papers*, vol. 41, no. 1, pp. 1–4, 2010.

[5] T. Okoshi, "Three-dimensional displays," *Proceedings of the IEEE*, vol. 68, no. 5, pp. 548–564, 1980.

[6] J.-Y. Son, V. V. Saveljev, Y.-J. Choi, J.-E. Bahn, S.-K. Kim, and H.-H. Choi, "Parameters for designing autostereoscopic imaging systems based on lenticular, parallax barrier, and integral photography plates," *Optical Engineering*, vol. 42, no. 11, pp. 3326–3334, 2003.

[7] J. Geng, "Three-dimensional display technologies," *Advances in Optics and Photonics*, vol. 5, no. 4, pp. 456–535, 2013.

[8] D. Smalley, E. Nygaard, K. Squire, J. Van Wagoner, J. Rasmussen, S. Gneiting, K. Qaderi, J. Goodsell, W. Rogers, M. Lindsey, *et al.*, "A photophoretic-trap volumetric display," *Nature*, vol. 553, no. 7689, p. 486, 2018.

[9] S. Tay, P.-A. Blanche, R. Voorakaranam, A. Tunç, W. Lin, S. Rokutanda, T. Gu, D. Flores, P. Wang, G. Li, *et al.*, "An updatable holographic three-dimensional display," *Nature*, vol. 451, no. 7179, pp. 694–698, 2008.

[10] G. Lippmann, "Epreuves reversibles donnant la sensation du relief," *Phys*, 1908.

[11] C. D. F. Winnek, "Apparatus for making a composite stereograph," Dec. 15 1936. US Patent 2,063,985.

[12] N. Davies, M. McCormick, and L. Yang, "Three-dimensional imaging systems: a new development," *Applied Optics*, vol. 27, no. 21, pp. 4520–4528, 1988.

[13] H. Arimoto and B. Javidi, "Integral three-dimensional imaging with digital reconstruction," *Optics Letters*, vol. 26, no. 3, pp. 157–159, 2001.

[14] J. Arai, F. Okano, H. Hoshino, and I. Yuyama, "Gradient-index lens-array method based on real-time integral photography for three-dimensional images," *Applied Optics*, vol. 37, no. 11, pp. 2034–2045, 1998.

[15] F. Okano, H. Hoshino, J. Arai, and I. Yuyama, "Real-time pickup method for a three-dimensional image based on integral photography," *Applied Optics*, vol. 36, no. 7, pp. 1598–1603, 1997.

[16] B. Javidi and F. Okano, *Three-dimensional television, video, and display technologies.* Springer Science & Business Media, 2002.

[17] A. Isaksen, L. McMillan, and S. J. Gortler, "Dynamically reparameterized light fields," in *Proceedings of the 27th Annual Conference on Computer Graphics and Interactive Techniques*, pp. 297–306, 2000.

[18] E. H. Adelson, J. R. Bergen, *et al.*, *The plenoptic function and the elements of early vision*, vol. 2. Vision and Modeling Group, Media Laboratory, Massachusetts Institute of Technology, 1991.

[19] R. Ng, M. Levoy, M. Brédif, G. Duval, M. Horowitz, P. Hanrahan, *et al.*, "Light field photography with a hand-held plenoptic camera," *Computer Science Technical Report CSTR*, vol. 2, no. 11, pp. 1–11, 2005.

[20] "https://www.lytro.com."

[21] "https://raytrix.de."

[22] J.-S. Jang and B. Javidi, "Improved viewing resolution of three-dimensional integral imaging by use of nonstationary micro-optics," *Optics Letters*, vol. 27, no. 5, pp. 324–326, 2002.

[23] S. Jung, J.-H. Park, H. Choi, and B. Lee, "Viewing-angle-enhanced integral three-dimensional imaging along all directions without mechanical movement," *Optics Express*, vol. 11, no. 12, pp. 1346–1356, 2003.

[24] P. Latorre-Carmona, E. Sánchez-Ortiga, X. Xiao, F. Pla, M. Martínez-Corral, H. Navarro, G. Saavedra, and B. Javidi, "Multispectral integral imaging acquisition and processing using a monochrome camera and a liquid crystal tunable filter," *Optics Express*, vol. 20, no. 23, pp. 25960–25969, 2012.

[25] A. Carnicer and B. Javidi, "Polarimetric 3d integral imaging in photon-starved conditions," *Optics Express*, vol. 23, no. 5, pp. 6408–6417, 2015.

[26] X. Xiao, B. Javidi, M. Martinez-Corral, and A. Stern, "Advances in three-dimensional integral imaging: sensing, display, and applications," *Applied Optics*, vol. 52, no. 4, pp. 546–560, 2013.

[27] Y. Zhao, X. Xiao, M. Cho, and B. Javidi, "Tracking of multiple objects in unknown background using bayesian estimation in 3d space," *JOSA A*, vol. 28, no. 9, pp. 1935–1940, 2011.

[28] K. Lynch, T. Fahringer, and B. Thurow, "Three-dimensional particle image velocimetry using a plenoptic camera," in *50th AIAA Aerospace Sciences Meeting including the New Horizons Forum and Aerospace Exposition*, p. 1056, 2012.

[29] X. Xiao, B. Javidi, G. Saavedra, M. Eismann, and M. Martinez-Corral, "Three-dimensional polarimetric computational integral imaging," *Optics Express*, vol. 20, no. 14, pp. 15481–15488, 2012.

[30] L. F. Rodríguez-Ramos, I. Montilla, J. Fernández-Valdivia, J. Trujillo-Sevilla, and J. Rodríguez-Ramos, "Concepts, laboratory, and telescope test results of the plenoptic camera as a wavefront sensor," in *Adaptive Optics Systems III*, vol. 8447, p. 844745, International Society for Optics and Photonics, 2012.

[31] A. Stern, Y. Yitzhaky, and B. Javidi, "Perceivable light fields: Matching the requirements between the human visual system and autostereoscopic 3-d displays," *Proceedings of the IEEE*, vol. 102, no. 10, pp. 1571–1587, 2014.

[32] N. Bedard, T. Shope, A. Hoberman, M. A. Haralam, N. Shaikh, J. Kovačević, N. Balram, and I. Tošić, "Light field otoscope

design for 3d in vivo imaging of the middle ear," *Biomedical Optics Express*, vol. 8, no. 1, pp. 260–272, 2017.

[33] H. Chen, V. Sick, M. A. Woodward, and D. Burke, "Human iris 3d imaging using a micro-plenoptic camera," in *Bio-Optics: Design and Application*, pp. BoW3A–6, Optical Society of America, 2017.

[34] J. Liu, D. Claus, T. Xu, T. Kessner, A. Herkommer, and W. Osten, "Light field endoscopy and its parametric description," *Optics Letters*, vol. 42, no. 9, pp. 1804–1807, 2017.

[35] A. Hassanfiroozi, Y.-P. Huang, B. Javidi, and H.-P. D. Shieh, "Hexagonal liquid crystal lens array for 3d endoscopy," *Optics Express*, vol. 23, no. 2, pp. 971–981, 2015.

[36] R. S. Decker, A. Shademan, J. D. Opfermann, S. Leonard, P. C. Kim, and A. Krieger, "Biocompatible near-infrared three-dimensional tracking system," *IEEE Transactions on Biomedical Engineering*, vol. 64, no. 3, pp. 549–556, 2017.

[37] N. C. Pégard, H.-Y. Liu, N. Antipa, M. Gerlock, H. Adesnik, and L. Waller, "Compressive light-field microscopy for 3d neural activity recording," *Optica*, vol. 3, no. 5, pp. 517–524, 2016.

[38] L. Cong, Z. Wang, Y. Chai, W. Hang, C. Shang, W. Yang, L. Bai, J. Du, K. Wang, and Q. Wen, "Rapid whole brain imaging of neural activity in freely behaving larval zebrafish (danio rerio)," *Elife*, vol. 6, p. e28158, 2017.

[39] A. Klein, T. Yaron, E. Preter, H. Duadi, and M. Fridman, "Temporal depth imaging," *Optica*, vol. 4, no. 5, pp. 502–506, 2017.

[40] T. Nöbauer, O. Skocek, A. J. Pernia-Andrade, L. Weilguny, F. M. Traub, M. I. Molodtsov, and A. Vaziri, "Video rate volumetric ca 2+ imaging across cortex using seeded iterative

demixing (sid) microscopy," *Nature Methods*, vol. 14, no. 8, p. 811, 2017.

[41] Y. Lv, H. Ma, Q. Sun, P. Ma, Y. Ning, and X. Xu, "Wavefront sensing based on partially occluded and extended scene target," *IEEE Photonics Journal*, vol. 9, no. 2, pp. 1–8, 2017.

[42] S. Komatsu, A. Markman, A. Mahalanobis, K. Chen, and B. Javidi, "Three-dimensional integral imaging and object detection using long-wave infrared imaging," *Applied Optics*, vol. 56, no. 9, pp. D120–D126, 2017.

[43] P. A. Coelho, J. E. Tapia, F. Pérez, S. N. Torres, and C. Saavedra, "Infrared light field imaging system free of fixed-pattern noise," *Scientific Reports*, vol. 7, no. 1, pp. 1–10, 2017.

[44] H. Hua and B. Javidi, "A 3d integral imaging optical see-through head-mounted display," *Optics Express*, vol. 22, no. 11, pp. 13484–13491, 2014.

[45] H. Huang and H. Hua, "High-performance integral-imaging-based light field augmented reality display using freeform optics," *Optics Express*, vol. 26, no. 13, pp. 17578–17590, 2018.

[46] A. Markman, J. Wang, and B. Javidi, "Three-dimensional integral imaging displays using a quick-response encoded elemental image array," *Optica*, vol. 1, no. 5, pp. 332–335, 2014.

[47] "http://real-eyes.eu/3d-displays/."

[48] D. J. Brady, M. E. Gehm, R. A. Stack, D. L. Marks, D. S. Kittle, D. R. Golish, E. Vera, and S. D. Feller, "Multiscale gigapixel photography," *Nature*, vol. 486, no. 7403, pp. 386–389, 2012.

[49] H. N. Fructuoso, M. Martínez-Corral, G. S. Tortosa, A. P. Marti, and B. Javidi, "Photoelastic analysis of partially occluded objects with an integral-imaging polariscope," *Journal of Display Technology*, vol. 10, no. 4, pp. 255–262, 2013.

[50] L. D. Elie and A. R. Gale, "System and method for inspecting road surfaces," Apr. 6 2017. US Patent App. 14/874,865.

[51] P. Drap, J.-P. Royer, M. M. Nawaf, M. Saccone, D. Merad, À. López-Sanz, J. Ledoux, and J. Garrabou, "Underwater photogrammetry, coded target and plenoptic technology: A set of tools for monitoring red coral in mediterranean sea in the framework of the 'perfect' project," *International Archives of the Photogrammetry, Remote Sensing and Spatial Information Sciences*, pp. 275–282, 2017.

[52] S.-H. Hong, J.-S. Jang, and B. Javidi, "Three-dimensional volumetric object reconstruction using computational integral imaging," *Optics Express*, vol. 12, no. 3, pp. 483–491, 2004.

[53] Y. S. Hwang and E.-S. Kim, "Perspective-variant reconstruction of a three-dimensional object along the depth direction with virtually generated elemental images by ray-based pixel mapping in integral-imaging," *Optics and Lasers in Engineering*, vol. 51, no. 7, pp. 797–807, 2013.

[54] L. McMillan and G. Bishop, "Plenoptic modeling: An image-based rendering system," in *Proceedings of the 22nd Annual Conference on Computer Graphics and Interactive Techniques*, pp. 39–46, Citeseer, 1995.

[55] J.-X. Chai, X. Tong, S.-C. Chan, and H.-Y. Shum, "Plenoptic sampling," in *Proceedings of the 27th Annual Conference on Computer Graphics and Interactive Techniques*, pp. 307–318, 2000.

[56] S. Kishk and B. Javidi, "Improved resolution 3d object sensing and recognition using time multiplexed computational integral imaging," *Optics Express*, vol. 11, no. 26, pp. 3528–3541, 2003.

[57] J.-H. Park, S. Jung, H. Choi, Y. Kim, and B. Lee, "Depth extraction by use of a rectangular lens array and one-dimensional

elemental image modification," *Applied Optics*, vol. 43, no. 25, pp. 4882–4895, 2004.

[58] G. Saavedra, R. Martínez-Cuenca, M. Martínez-Corral, H. Navarro, M. Daneshpanah, and B. Javidi, "Digital slicing of 3d scenes by fourier filtering of integral images," *Optics Express*, vol. 16, no. 22, pp. 17154–17160, 2008.

[59] M. Cho and B. Javidi, "Three-dimensional visualization of objects in turbid water using integral imaging," *Journal of Display Technology*, vol. 6, no. 10, pp. 544–547, 2010.

[60] M. Levoy, R. Ng, A. Adams, M. Footer, and M. Horowitz, "Light field microscopy," *ACM Transactions on Graphics (TOG)*, vol. 25, no. 3, pp. 924–934, 2006.

[61] E. Cuche, P. Marquet, and C. Depeursinge, "Simultaneous amplitude-contrast and quantitative phase-contrast microscopy by numerical reconstruction of fresnel off-axis holograms," *Applied Optics*, vol. 38, no. 34, pp. 6994–7001, 1999.

[62] E. Sánchez-Ortiga, A. Doblas, G. Saavedra, M. Martínez-Corral, and J. Garcia-Sucerquia, "Off-axis digital holographic microscopy: practical design parameters for operating at diffraction limit," *Applied Optics*, vol. 53, no. 10, pp. 2058–2066, 2014.

[63] J. Pawley, *Handbook of biological confocal microscopy*, vol. 236. Springer Science & Business Media, 2006.

[64] M. Martínez-Corral and G. Saavedra, "The resolution challenge in 3d optical microscopy," *Progress in Optics*, vol. 53, p. 1, 2009.

[65] M. Gu and C. Sheppard, "Confocal fluorescent microscopy with a finite-sized circular detector," *JOSA A*, vol. 9, no. 1, pp. 151–153, 1992.

[66] T. Wilson, *Confocal microscopy*. Academic press, 1990.

[67] E. Sánchez-Ortiga, C. J. Sheppard, G. Saavedra, M. Martínez-Corral, A. Doblas, and A. Calatayud, "Subtractive imaging in confocal scanning microscopy using a ccd camera as a detector," *Optics Letters*, vol. 37, no. 7, pp. 1280–1282, 2012.

[68] M. A. Neil, R. Juškaitis, and T. Wilson, "Method of obtaining optical sectioning by using structured light in a conventional microscope," *Optics Letters*, vol. 22, no. 24, pp. 1905–1907, 1997.

[69] M. G. Gustafsson, "Surpassing the lateral resolution limit by a factor of two using structured illumination microscopy," *Journal of Microscopy*, vol. 198, no. 2, pp. 82–87, 2000.

[70] A. G. York, S. H. Parekh, D. Dalle Nogare, R. S. Fischer, K. Temprine, M. Mione, A. B. Chitnis, C. A. Combs, and H. Shroff, "Resolution doubling in live, multicellular organisms via multifocal structured illumination microscopy," *Nature Methods*, vol. 9, no. 7, pp. 749–754, 2012.

[71] E. H. Stelzer, K. Greger, and E. Reynaud, *Light Sheet Based Fluorescence Microscopy: Principles and Practice*. Wiley-Vch, 2011.

[72] P. A. Santi, "Light sheet fluorescence microscopy: a review," *Journal of Histochemistry & Cytochemistry*, vol. 59, no. 2, pp. 129–138, 2011.

[73] I. Moon and B. Javidi, "Three-dimensional identification of stem cells by computational holographic imaging," *Journal of the Royal Society Interface*, vol. 4, no. 13, pp. 305–313, 2007.

[74] S. Ebrahimi, M. Dashtdar, E. Sánchez-Ortiga, M. Martínez-Corral, and B. Javidi, "Stable and simple quantitative phase-contrast imaging by fresnel biprism," *Applied Physics Letters*, vol. 112, no. 11, p. 113701, 2018.

[75] J.-c. Li and P. Picart, "Digital holographic interferometry and its applications," *Digital Holography*, pp. 271–318, 2012.

[76] M. Martinez-Corral, P.-Y. Hsieh, A. Doblas, E. Sanchez-Ortiga, G. Saavedra, and Y.-P. Huang, "Fast Axial-Scanning Wide-field Microscopy With Constant Magnification and Resolution," *Journal of Display Technology*, vol. 11, pp. 913–920, Nov. 2015.

[77] B. F. Grewe, F. F. Voigt, M. van't Hoff, and F. Helmchen, "Fast two-layer two-photon imaging of neuronal cell populations using an electrically tunable lens," *Biomedical Optics Express*, vol. 2, no. 7, pp. 2035–2046, 2011.

[78] F. O. Fahrbach, F. F. Voigt, B. Schmid, F. Helmchen, and J. Huisken, "Rapid 3d light-sheet microscopy with a tunable lens," *Optics Express*, vol. 21, no. 18, pp. 21010–21026, 2013.

[79] J. M. Jabbour, B. H. Malik, C. Olsovsky, R. Cuenca, S. Cheng, J. A. Jo, Y.-S. L. Cheng, J. M. Wright, and K. C. Maitland, "Optical axial scanning in confocal microscopy using an electrically tunable lens," *Biomedical Optics Express*, vol. 5, no. 2, pp. 645–652, 2014.

[80] J.-S. Jang and B. Javidi, "Three-dimensional integral imaging of micro-objects," *Optics Letters*, vol. 29, no. 11, pp. 1230–1232, 2004.

[81] Y.-T. Lim, J.-H. Park, K.-C. Kwon, and N. Kim, "Resolution-enhanced integral imaging microscopy that uses lens array shifting," *Optics Express*, vol. 17, no. 21, pp. 19253–19263, 2009.

[82] A. Llavador, E. Sánchez-Ortiga, J. C. Barreiro, G. Saavedra, and M. Martínez-Corral, "Resolution enhancement in integral microscopy by physical interpolation," *Biomedical Optics Express*, vol. 6, no. 8, pp. 2854–2863, 2015.

[83] M. Broxton, L. Grosenick, S. Yang, N. Cohen, A. Andalman, K. Deisseroth, and M. Levoy, "Wave optics theory and 3-d

deconvolution for the light field microscope," *Optics Express*, vol. 21, no. 21, pp. 25418–25439, 2013.

[84] K.-C. Kwon, J.-S. Jeong, M.-U. Erdenebat, Y.-L. Piao, K.-H. Yoo, and N. Kim, "Resolution-enhancement for an orthographic-view image display in an integral imaging microscope system," *Biomedical Optics Express*, vol. 6, no. 3, pp. 736–746, 2015.

[85] X. Lin, J. Wu, G. Zheng, and Q. Dai, "Camera array based light field microscopy," *Biomedical Optics Express*, vol. 6, no. 9, pp. 3179–3189, 2015.

[86] A. Llavador, J. Sola-Pikabea, G. Saavedra, B. Javidi, and M. Martínez-Corral, "Resolution improvements in integral microscopy with fourier plane recording," *Optics Express*, vol. 24, no. 18, pp. 20792–20798, 2016.

[87] G. Scrofani, J. Sola-Pikabea, A. Llavador, E. Sanchez-Ortiga, J. Barreiro, G. Saavedra, J. Garcia-Sucerquia, and M. Martínez-Corral, "Fimic: design for ultimate 3d-integral microscopy of in-vivo biological samples," *Biomedical Optics Express*, vol. 9, no. 1, pp. 335–346, 2018.

[88] J. W. Goodman, *Introduction to Fourier optics.* Roberts and Company Publishers, 2005.

[89] H. Navarro, E. Sánchez-Ortiga, G. Saavedra, A. Llavador, A. Dorado, M. Martínez-Corral, and B. Javidi, "Non-homogeneity of lateral resolution in integral imaging," *Journal of Display Technology*, vol. 9, no. 1, pp. 37–43, 2013.

[90] A. Llavador, G. Scrofani, G. Saavedra, and M. Martinez-Corral, "Large depth-of-field integral microscopy by use of a liquid lens," *Sensors*, vol. 18, no. 10, p. 3383, 2018.

[91] A. Doblas, E. Sánchez-Ortiga, G. Saavedra, J. Sola-Pikabea, M. Martínez-Corral, P.-Y. Hsieh, and Y.-P. Huang, "Three-dimensional microscopy through liquid-lens axial scanning," in *Three-Dimensional Imaging, Visualization, and Display 2015*, vol. 9495, p. 949503, International Society for Optics and Photonics, 2015.

[92] M. Martínez-Corral and B. Javidi, "Fundamentals of 3d imaging and displays: a tutorial on integral imaging, light-field, and plenoptic systems," *Advances in Optics and Photonics*, vol. 10, no. 3, pp. 512–566, 2018.

[93] A. Stefanoiu, J. Page, P. Symvoulidis, G. G. Westmeyer, and T. Lasser, "Artifact-free deconvolution in light field microscopy," *Optics Express*, vol. 27, no. 22, pp. 31644–31666, 2019.

[94] G. Scrofani, J. Sola-Pikabea, A. Llavador, E. Sánchez-Ortiga, J. Barreiro, J. Garcia-Sucerquia, N. Incardona, and M. Martinez-Corral, "3d integral microscopy based in far-field detection," in *Three-Dimensional Imaging, Visualization, and Display 2018*, vol. 10666, p. 106660Z, International Society for Optics and Photonics, 2018.

[95] M. Levoy, "Light fields and computational imaging," *Computer*, vol. 39, no. 8, pp. 46–55, 2006.

[96] C. Chen, Y. Lu, and M. Su, "Light field based digital refocusing using a dslr camera with a pinhole array mask," in *2010 IEEE International Conference on Acoustics, Speech and Signal Processing*, pp. 754–757, 2010.

[97] L. Tian and L. Waller, "3d intensity and phase imaging from light field measurements in an led array microscope," *Optica*, vol. 2, no. 2, pp. 104–111, 2015.

[98] S. Moreschini, G. Scrofani, R. Brcgovic, G. Saavedra, and A. Gotchev, "Continuous refocusing for integral microscopy with fourier plane recording," in *2018 26th European Signal Processing Conference (EUSIPCO)*, pp. 216–220, IEEE, 2018.

[99] Y. Li, G. Scrofani, M. Sjöström, and M. Martinez-Corral, "Area-based depth estimation for monochromatic feature-sparse orthographic capture," in *2018 26th European Signal Processing Conference (EUSIPCO)*, pp. 206–210, IEEE, 2018.

[100] M. Subbarao and J.-K. Tyan, "Selecting the optimal focus measure for autofocusing and depth-from-focus," *IEEE Transactions on Pattern Analysis and Machine Intelligence*, vol. 20, no. 8, pp. 864–870, 1998.

[101] S. K. Nayar and Y. Nakagawa, "Shape from focus," *IEEE Transactions on Pattern Analysis and Machine Intelligence*, vol. 16, no. 8, pp. 824–831, 1994.

[102] H.-H. Nagel and W. Enkelmann, "An investigation of smoothness constraints for the estimation of displacement vector fields from image sequences," *IEEE Transactions on Pattern Analysis and Machine Intelligence*, no. 5, pp. 565–593, 1986.

[103] O. Schreer, P. Kauff, and T. Sikora, *3D Videocommunication: Algorithms, concepts and real-time systems in human centred communication.* John Wiley & Sons, 2005.

[104] E. Sánchez-Ortiga, A. Llavador, G. Saavedra, J. García-Sucerquia, and M. Martínez-Corral, "Optical sectioning with a wiener-like filter in fourier integral imaging microscopy," *Applied Physics Letters*, vol. 113, no. 21, p. 214101, 2018.

[105] S. C. Park, M. K. Park, and M. G. Kang, "Super-resolution image reconstruction: a technical overview," *IEEE Signal Processing Magazine*, vol. 20, no. 3, pp. 21–36, 2003.

[106] S. Farsiu, D. Robinson, M. Elad, and P. Milanfar, "Advances and challenges in super-resolution," *International Journal of Imaging Systems and Technology*, vol. 14, no. 2, pp. 47–57, 2004.

[107] J. Tian and K.-K. Ma, "A survey on super-resolution imaging," *Signal, Image and Video Processing*, vol. 5, no. 3, pp. 329–342, 2011.

[108] T. E. Bishop and P. Favaro, "The light field camera: Extended depth of field, aliasing, and superresolution," *IEEE Transactions on Pattern Analysis and Machine Intelligence*, vol. 34, no. 5, pp. 972–986, 2011.

[109] S. Wanner and B. Goldluecke, "Variational light field analysis for disparity estimation and super-resolution," *IEEE Transactions on Pattern Analysis and Machine Intelligence*, vol. 36, no. 3, pp. 606–619, 2013.

[110] K. Sauer and J. Allebach, "Iterative reconstruction of bandlimited images from nonuniformly spaced samples," *IEEE Transactions on Circuits and Systems*, vol. 34, no. 12, pp. 1497–1506, 1987.

[111] K. Gröchenig, "Reconstruction algorithms in irregular sampling," *Mathematics of Computation*, vol. 59, no. 199, pp. 181–194, 1992.

[112] K. Gröchenig and T. Strohmer, "Numerical and theoretical aspects of nonuniform sampling of band-limited images," in *Nonuniform Sampling*, pp. 283–324, Springer, 2001.

[113] W. H. Richardson, "Bayesian-based iterative method of image restoration," *JOSA A*, vol. 62, no. 1, pp. 55–59, 1972.

[114] L. B. Lucy, "An iterative technique for the rectification of observed distributions," *The Astronomical Journal*, vol. 79, p. 745, 1974.

[115] J. Žbontar and Y. LeCun, "Stereo matching by training a convolutional neural network to compare image patches," *The Journal of Machine Learning Research*, vol. 17, no. 1, pp. 2287–2318, 2016.

[116] S. Pertuz, D. Puig, and M. A. Garcia, "Analysis of focus measure operators for shape-from-focus," *Pattern Recognition*, vol. 46, no. 5, pp. 1415–1432, 2013.

[117] "https://www.blender.org."

[118] T. Horio and H. Hotani, "Visualization of the dynamic instability of individual microtubules by dark-field microscopy," *Nature*, vol. 321, no. 6070, pp. 605–607, 1986.

[119] E. Sánchez-Ortiga, G. Scrofani, G. Saavedra, and M. Martinez-Corral, "Optical sectioning microscopy through single-shot lightfield protocol," *IEEE Access*, vol. 8, pp. 14944–14952, 2020.

List of publications

Main articles

[**I**]   **G. Scrofani**, J. Sola-Pikabea, A. Llavador, E. Sanchez-Ortiga, J.C. Barreiro, G. Saavedra, J. Garcia-Sucerquia, and M. Martinez-Corral. FIMic: design for ultimate 3D-integral microscopy of in-vivo biological samples. Biomed. Opt. Express 9, 335-346 (2018).

[**II**]   A. Llavador, **G. Scrofani**, G. Saavedra, and M. Martinez-Corral. Large depth-of-field integral microscopy by use of a liquid lens. Sensors 18, 3383 (2018).

[**III**]   L. Palmieri, **G. Scrofani**, N. Incardona, G. Saavedra, M. Martínez-Corral, and R. Koch. Robust depth estimation for light field microscopy. Sensors, 19, 0500 (2019).

[**IV**]   E. Sanchez-Ortiga, **G. Scrofani**, G. Saavedra, and M. Martinez-Corral. Optical sectioning microscopy through single-shot Lightfield protocol, IEEE Access 8, 14944-14952 (2020).

Contribution articles

[V]   A. Stefanoiu, G. Scrofani, G. Saavedra, M. Martinez-Corral, and T. Lasser, "What about super-resolution in fourier lightfield microscopy?," Optics Express, vol. 28, pp. 16554-16568 (2020).

Patents

[VI]   **Inventors**: M. Martínez-Corral, G. Saavedra, **G. Scrofani**, A. Tolosa and J. García-Sucerquia **Title**: Ocular opto-electrónico para producir imágenes plenópticas **Priority Number**: P201830812 (Aug. 2018) **Applicant**: Universidad de Valencia y Universidad Nacional de Colombia. **Licensed by**: DOIT-PLENOPTC S.L.

Conference participations

[VII]   **G. Scrofani**, J. Sola-Pikabea, J.C. Barreiro, M. Martinez-Corral, G. Saavedra, "Three dimensional imaging through Fourier-domain Integral Microscopy." Focus on Microscopy, Bordeaux (France), April 2017.

[VIII]   J. Sola-Pikabea, **G. Scrofani**, A. Llavador, J.C. Barreiro, M. Martínez Corral, and G. Saavedra, "Dark-Field Imaging with an Integral Microscope." Focus on Microscopy, Bordeaux (France), April 2017.

[IX]   M. Martínez-Corral, J.C. Barreiro, A. Llavador, E. Sánchez-Ortiga, J. Sola-Pikabea, **G. Scrofani**, and G. Saavedra. "Integral imaging with Fourier-plane recording" Proc. SPIE 10219, 10219-0B (2017).

[**X**]   M. Martinez-Corral, J.C.Barreiro, A. Llavador , E. Sánchez-Ortiga, J. Sola-Pikabea, **G. Scrofani**, G. Saavedra y B. Javidi, "Three-dimensional imaging through Fourier-domain Integral Microscopy". III International Conference on Applications in Optics and Photonics (AOP 2017). Faro (Portugal), May 2017.

[**XI**]   Li, Y., **Scrofani, G.**, Sjöström, M., and Martinez-Corral, M. (2018, September). Area-Based Depth Estimation for Monochromatic Feature-Sparse Orthographic Capture. In 2018 26th European Signal Processing Conference (EUSIPCO) (pp. 206-210). IEEE.

[**XII**]   Moreschini, S., **Scrofani, G.**, Brcgovic, R., Saavedra, G., and Gotchev, A. (2018, September). Continuous Refocusing for Integral Microscopy with Fourier Plane Recording. In 2018 26th European Signal Processing Conference (EUSIPCO) (pp. 216-220). IEEE.

[**XIII**]   **G. Scrofani**, J. Sola-Pikabea, A. Llavador, E. Sanchez-Ortiga, J.C. Barreiro, J. Garcia-Sucerquia, N. Incardona, and M. Martinez-Corral. 3D integral microscopy based in far-field detection. Proc. SPIE 10666, 0Z (2018).

[**XIV**]   **G. Scrofani**, J. Sola-Pikabea, G. Saavedra, A. Llavador, E. SanchezOrtiga, J.C. Barreiro, J. GarciaSucerquia y M. Martínez-Corral, "Microscopia Integral de Campo Lejano". Reunion Nacional de Optica (RNO2018). Castellon de la Plana (Spain), July 2018.

[**XV**]   **G. Scrofani**, J. Sola-Pikabea, E. Sánchez-Ortiga, J. Carlos Barreiro, M. Martínez-Corral, and G. Saavedra. "Phase imaging of 3D specimen through darkfield FiMic". San Francisco (USA) Electronic Imaging (EI2019), January 2019.

[**XVI**]   **G. Scrofani**, N. Incardona, G. Saavedra, M. Martinez-Corral. "Real-Time 3D Display for LightField Microscopy". Focus on Microscopy (FOM2019). London (UK). April 2019.

[**XVII**]   **G. Scrofani**. "FiMic: Fourier Plane Integral Microscope, a Light-Field Microscope and Its Applications". European Light Field Imaging (ELFI2019). Borovets (Bulgaria). June 2019.

[**XVIII**]   A. Stefanoiu, **G. Scrofani**, G. Saavedra, M. Martínez-Corral and T. Lasser, "Deconvolution in Fourier integral microscopy". In Computational Imaging V (Vol. 11396, p. 113960I). International Society for Optics and Photonics, May 2020